AFRL-OSR-VA-TR-2015-0130

MODELING AND ANALYSIS TOOLS FOR NONLINEAR MECHANICAL SYSTEMS

ANDREW DICK
WILLIAM MARSH RICE UNIV HOUSTON TX

03/23/2015
Final Report

Air Force Research Laboratory
AF Office Of Scientific Research (AFOSR)/ RTA
Arlington, Virginia 22203
Air Force Materiel Command

REPORT DOCUMENTATION PAGE

Form Approved
OMB No. 0704-0188

PLEASE DO NOT RETURN YOUR FORM TO THE ABOVE ORGANIZATION.

1. REPORT DATE *(DD-MM-YYYY)*	2. REPORT TYPE	3. DATES COVERED *(From - To)*
16-03-2015	Final Report	July 1, 2011 - June 30, 2014

4. TITLE AND SUBTITLE
Modeling and Analysis Tools for Linear and Nonlinear Mechanical Systems Subjected to Extreme Impulsive Loading

5a. CONTRACT NUMBER

5b. GRANT NUMBER
FA9550-11-1-0108

5c. PROGRAM ELEMENT NUMBER

6. AUTHOR(S)
A. J. Dick

5d. PROJECT NUMBER

5e. TASK NUMBER

5f. WORK UNIT NUMBER

7. PERFORMING ORGANIZATION NAME(S) AND ADDRESS(ES)
Department of Mechanical Engineering
Rice University
Houston, TX 77005-1827

8. PERFORMING ORGANIZATION REPORT NUMBER

9. SPONSORING/MONITORING AGENCY NAME(S) AND ADDRESS(ES)
Dr. David Stargel
Program Manager, Multi-Scale Structural Mechanics and Prognosis
AFOSR/RTA
875 North Randolph St, Suite 325, Room 3112
Arlington VA 22203-1768

10. SPONSOR/MONITOR'S ACRONYM(S)

11. SPONSOR/MONITOR'S REPORT NUMBER(S)

12. DISTRIBUTION/AVAILABILITY STATEMENT
Distribution A

13. SUPPLEMENTARY NOTES

14. ABSTRACT
The extreme impact loading (high amplitude and short durations) can result in wave propagation with significant nonlinear characteristics. The focus of this work was the development of high fidelity modeling and analysis methods for studying this nonlinear behavior. The Alternating Frequency-Time Finite Element Method was developed from the spectral finite element method (SFEM) in order to expand its high fidelity performance to study nonlinear wave propagation. Later efforts produced the Alternating Wavelet-Time Finite Element Method by using a wavelet basis. A practical force identification scheme was also developed by using SFEM to determine both temporal and spatial information about an impact load by using only a small number of sensors. The force identification scheme was also developed by using SFEM to determine both temporal and spatial information about an impact load by using only a small number of sensors. These numerical simulation techniques and force identification methods provide the means to gain new insight into the effects of extreme impact loading on structures. This improved understanding can be used to design new structures and to better understand how they will perform under severe conditions.

15. SUBJECT TERMS
Impact Response, Nonlinear Wave Propagation, Spectral Finite Element Method, Wavelets, Force Identification

16. SECURITY CLASSIFICATION OF:			17. LIMITATION OF ABSTRACT	18. NUMBER OF PAGES	19a. NAME OF RESPONSIBLE PERSON
a. REPORT	b. ABSTRACT	c. THIS PAGE			A. J. Dick
					19b. TELEPHONE NUMBER *(Include area code)* (713) 348-5259

Reset

INSTRUCTIONS FOR COMPLETING SF 298

1. REPORT DATE. Full publication date, including day, month, if available. Must cite at least the year and be Year 2000 compliant, e.g. 30-06-1998; xx-06-1998; xx-xx-1998.

2. REPORT TYPE. State the type of report, such as final, technical, interim, memorandum, master's thesis, progress, quarterly, research, special, group study, etc.

3. DATES COVERED. Indicate the time during which the work was performed and the report was written, e.g., Jun 1997 - Jun 1998; 1-10 Jun 1996; May - Nov 1998; Nov 1998.

4. TITLE. Enter title and subtitle with volume number and part number, if applicable. On classified documents, enter the title classification in parentheses.

5a. CONTRACT NUMBER. Enter all contract numbers as they appear in the report, e.g. F33615-86-C-5169.

5b. GRANT NUMBER. Enter all grant numbers as they appear in the report, e.g. AFOSR-82-1234.

5c. PROGRAM ELEMENT NUMBER. Enter all program element numbers as they appear in the report, e.g. 61101A.

5d. PROJECT NUMBER. Enter all project numbers as they appear in the report, e.g. 1F665702D1257; ILIR.

5e. TASK NUMBER. Enter all task numbers as they appear in the report, e.g. 05; RF0330201; T4112.

5f. WORK UNIT NUMBER. Enter all work unit numbers as they appear in the report, e.g. 001; AFAPL30480105.

6. AUTHOR(S). Enter name(s) of person(s) responsible for writing the report, performing the research, or credited with the content of the report. The form of entry is the last name, first name, middle initial, and additional qualifiers separated by commas, e.g. Smith, Richard, J, Jr.

7. PERFORMING ORGANIZATION NAME(S) AND ADDRESS(ES). Self-explanatory.

8. PERFORMING ORGANIZATION REPORT NUMBER. Enter all unique alphanumeric report numbers assigned by the performing organization, e.g. BRL-1234; AFWL-TR-85-4017-Vol-21-PT-2.

9. SPONSORING/MONITORING AGENCY NAME(S) AND ADDRESS(ES). Enter the name and address of the organization(s) financially responsible for and monitoring the work.

10. SPONSOR/MONITOR'S ACRONYM(S). Enter, if available, e.g. BRL, ARDEC, NADC.

11. SPONSOR/MONITOR'S REPORT NUMBER(S). Enter report number as assigned by the sponsoring/ monitoring agency, if available, e.g. BRL-TR-829; -215.

12. DISTRIBUTION/AVAILABILITY STATEMENT. Use agency-mandated availability statements to indicate the public availability or distribution limitations of the report. If additional limitations/ restrictions or special markings are indicated, follow agency authorization procedures, e.g. RD/FRD, PROPIN, ITAR, etc. Include copyright information.

13. SUPPLEMENTARY NOTES. Enter information not included elsewhere such as: prepared in cooperation with; translation of; report supersedes; old edition number, etc.

14. ABSTRACT. A brief (approximately 200 words) factual summary of the most significant information.

15. SUBJECT TERMS. Key words or phrases identifying major concepts in the report.

16. SECURITY CLASSIFICATION. Enter security classification in accordance with security classification regulations, e.g. U, C, S, etc. If this form contains classified information, stamp classification level on the top and bottom of this page.

17. LIMITATION OF ABSTRACT. This block must be completed to assign a distribution limitation to the abstract. Enter UU (Unclassified Unlimited) or SAR (Same as Report). An entry in this block is necessary if the abstract is to be limited.

Modeling and Analysis Tools for Linear and Nonlinear Mechanical Systems Subjected to Extreme Impulsive Loading

AFOSR GRANT FA9550-11-1-0108

A. J. Dick
Department of Mechanical Engineering
William Marsh Rice University
Houston, TX 77005-1827

1 Summary

The extreme impact loading consider in this work consists of high amplitude loads with short durations which can result in high frequency content. These conditions can result in wave propagation with significant nonlinear characteristics. With the use of conventional, linear high fidelity methods, the effects of the nonlinearity can be overlooked and its influence on the structure will not be known. The focus of this work was the development of high fidelity modeling and analysis methods for studying this nonlinear behavior. The Alternating Frequency-Time Finite Element Method (AFT-FEM) was developed from the spectral finite element method (SFEM) in order to expand its high fidelity performance to study nonlinear wave propagation. Later efforts produced the Alternating Wavelet-Time Finite Element Method (AWT-FEM) by using a wavelet basis. A wavelet basis is better conditioned for studying localized and transient signal characteristics such as those encountered in impact loading and, as a result, AWT-FEM provides further improvements beyond AFT-FEM. A practical force identification scheme was also developed by using SFEM to determine both temporal and spatial information about an impact load by using only a small number of sensors. The force identification scheme was first applied to linear systems and then, by using the concepts developed for AWT-FEM, it was extended to be able to perform force identification for nonlinear systems. These numerical simulation techniques and force identification methods provide the means to gain new insight into the effects of extreme impact loading on structures. This improved understanding can them be used to design new systems and structures and to better understand how they will perform under severe conditions.

Key words: Impact Response, Nonlinear Wave Propagation, Spectral Finite Element Method, Wavelets, Force Identification

2 Introduction

In the majority of traditional scientific and technological applications, wave propagation in solid structures is bounded by the elastic limit and a linear approximation is often adopted. However, as the exploration is entering into more advanced fields like new materials, extreme working environments, and high fidelity analysis, nonlinearity can be introduced in various ways and can become a crucial factor that must not be neglected. In the past decade, facilitated by the development of numerical techniques and high performance computers, significant progress has been made in the study of nonlinear elastic wave propagation for applications including biomedical analysis [1], nondestructive evaluation [2], and seismic motion analysis [3].

In many military and civil applications, nonlinear mechanical wave propagation occurs through structural components that can be approximated as rods, beams, or plates. For example, in the force identification of aircraft through impact wave analysis, the impact load often has a high amplitude with a short duration, where high frequency content in the response will significantly strengthen the influence of the nonlinear properties. The wings of the aircraft can be approximated as a beam or plate structure with a geometric nonlinearity. Another example is in the monitoring and control of drill strings in the oilfield. Drill strings can be modeled as long geometrically nonlinear beams with different cross sections and material properties [4]. Elastic waves caused by impacts with the wellbore and stress waves in the mud flow can be used to control the stability [5]. A third example is in the dynamics of high-speed and high-precision parallel robots [6]. Each link of the robot can be modeled as a beam undergoing large deformation. For these systems and many other, exact solutions of linear wave equations for rod, beam, and plate structures are known [7] and analytical relationships in the nonlinear wave equation are also well established [8]. Incorporating those results with a general numerical framework will greatly improve the computational performance and provide significantly improved accuracy.

For these systems and many other, exact solutions of linear wave equations for rod, beam, and plate structures are known [7] and analytical relationships in the nonlinear wave equation are also well established [8]. Incorporating those results with a general numerical framework will greatly improve the computational performance and provide significantly improved accuracy.

2.1 Modeling Nonlinear Wave Propagation

Based on the specific nature of nonlinear elastic wave propagation, a good numerical technique should fulfill three requirements. (1) Provide the means to predict high fidelity responses - Nonlinear phenomenon can be accurately captured in the response and available for further analysis. (2) Provide high computational efficiency - The method should take advantage of current computation technology to ensure studying larger models is not computational prohibitive. (3) Be flexible - The method should be able to be applied to various structures for a range of working constraints.

A comparison of existing methods is shown in Table. 1. There are five examination criteria: (1) high fidelity performance, (2) applicability to study linear behavior, (3) applicability to study nonlinear behavior, (4) ability to represent physically realistic boundary constraints, and (5) parallel computing compatibility. The check mark (✓) indicates that the criterion is satisfied, the dash mark (−) indicates the criterion is partially satisfied, and the X mark (×) indicates that the criterion is not satisfied. The AFT-FEM and AWT-FEM developed in this work are included for comparison.

Table 1: Comparison of different methods.

Methods	High Fidelity	Linear	Nonlinear	Boundary	Parallel
TFEM [9]	×	✓	✓	✓	−
MTFEM [10]	✓	✓	✓	✓	−
SFEM [11]	✓	✓	×	−	✓
WSFEM [12]	✓	✓	×	✓	✓
AFT-FEM	✓	✓	✓	−	✓
AWT-FEM	✓	✓	✓	✓	✓

The finite element method (FEM) [9] has been widely applied to study structural dynamics and has developed into a class of numerical methods with various time integration and space discretization techniques. In Table 1, the time-domain FEM (TFEM) refers to a standardized procedure composed of a serial time-integration technique like the Newmark method, an iteration approach like the Newton-Raphson method to address nonlinearity, and a standard finite element space discretization to approximate the geometry. Other modified versions of FEM with various time-integration techniques like space-time finite element method [13] is not considered here. TFEM can be used to solve both linear and nonlinear problems with physically realistic boundary conditions and complex geometries. However, for transient wave propagation,

especially those caused by impact loading with high frequency content, responses predicted with this method can exhibit spurious oscillations which results from erroneously introduced numerical dispersion and dissipation [10, 14]. This error will accumulate as the wave travels along a structure and significantly distort the response unless an extremely fine meshing is adopted to capture the sharp gradient change in the wave shape. Also, due to the serial nature of the Newmark method, TFEM cannot be directly incorporated into a parallel computing framework. Speed-up procedures are needed to make it compatible with a parallel computational framework.

In order to solve the spurious oscillation error and obtain a high fidelity response, many modified time-domain finite element methods (MTFEM) have been developed by using more advanced interpolation functions [10, 15]. The spectral element method (SEM) first proposed by Patera [16] in fluid dynamics has been adapted to study 1D linear wave propagation in solid structures [15]. In SEM, high order polynomials have been chosen as local shape functions and a high degree of accuracy in the response can be observed. An application of SEM to study 1D nonlinear wave propagation in a rod was reported in [17]. Even though theoretically SEM can be adapted to solve nonlinear problems, other related works are surprisingly rare in the literature. Ham and Bathe proposed another modified method using low-order polynomials enriched with harmonic functions [10]. A specific scheme has also been designed to overcome ill-conditioning. This method can be used to solve both linear and materially nonlinear systems, but may encounter challenges for systems with geometric nonlinearities. Extra efforts on reformation are needed to make these methods compatible for the parallel computing framework.

Another class of methods transforms the model and solution procedure into a spectral domain. A typical example is the fast Fourier transform (FFT)-based spectral finite element method (SFEM) proposed by Doyle [7, 11]. In the literature, there is some confusion over the terms SFEM and SEM [15]. Here, SFEM specifically refers to the Fourier-based method developed by Doyle. For linear problems, SFEM uses exact wave solution as frequency-dependent shape functions and only one element is required to obtain highly accurate responses for a given position in a structural component like a rod or a beam. For a structure like a frame or a truss, an element-based procedure can be adopted at each independent frequency. This makes the method inherently suitable for parallel computing. With the incorporation of the exact analytical wave solutions, the capacity for parallel computing and the fast computational performance of FFT, the SFEM can be utilized as a real-time method to obtain high fidelity responses to impacts with high frequency content. Various applications on linear 1D and 2D problems can be found in Gopalakrishnan and

Lee's works [18, 19]. However, this method has two major drawbacks. First, the periodic nature of the basis functions used for the Fourier transform can result in wrap-around issues in which the signal outside the time-window will become wrapped around to the beginning of the signal sequence. Semi-infinite elements (non-reflecting boundary condition) are often added at the ends of a structure to leak energy out of the system. For other types of boundary conditions, additional damping combined with a longer time-window is required. This greatly deteriorates the computational performance of SFEM when it is applied to study wave propagation in structures with physically realistic boundary constraints. Second, nonlinear terms often result in convolution terms in the frequency-domain, which are computationally prohibitive to calculate with iterative procedures. This makes SFEM not directly applicable for nonlinear systems.

In order to avoid the wrap-around issue of SFEM, Mitra and Gopalakrishnan developed a wavelet-based spectral finite element method (WSFEM) [12]. Instead of using FFT, a discrete wavelet transform (DWT) on the sampling scale was adopted to transform the linear wave equation into a wavelet-domain where each wavelet point represents a shifting along time axis. A wavelet extrapolation technique was also incorporated to represent non-periodic boundary conditions [20]. WSFEM successfully circumvented the wrap-around issue and can also be incorporated into a parallel computing framework after being uncoupled through an eigenvalue analysis. Applications to linear wave propagation in composite and nano-composite structures were reported in [21]. An adaptation of the wavelet transformation technique in WSFEM with SEM spatial interpolation was also applied to 2D and 3D linear elastic waves [22, 23]. Similar to SFEM, WSFEM cannot be directly applied to study nonlinear systems.

An intuitive solution to deal with the nonlinear problem in frequency-domain methods is to transform the calculation of the nonlinear terms back to the time-domain. An alternating frequency-time iterative framework is needed to transform the result of the nonlinear calculation into the frequency-domain, solve for the linear solution by using SFEM, and then return to the time-domain to calculate new values of the nonlinear terms for the next iteration. This framework was first proposed by Cameron [24]. A combination of it with the SFEM was performed by Lee [25] to study 1D nonlinear blood flow in human arteries.

2.2 Force Identification

Indirect methods for impact force identification have attracted researchers due to the nonlinearity of the impact problem and complexity of impact incidents [26, 27, 28, 29]. Numerous techniques have been developed which uses inverse methods for impact force identification. Some common techniques for force identification are the deconvolution method [26, 27], state variable formulation [30], the sum of weighted accelerations [31], and the spectral finite element method [12]. The most popular method is the deconvolution technique which uses the assumption of a linear response in order to allow for the application of the convolution integral to identify the force information. For linear systems, the convolution integral of a system's impulse response and the applied force results in the response of the system. This technique has been applied in both the time-domain [26] and the frequency-domain [32].

In a study by Doyle, a time-domain deconvolution technique was successfully developed in order to experimentally obtain dynamic contact laws [26]. Response behavior was monitored by using strain gages affixed to a beam structure and the impulsive load was applied by using a pendulous ball. In other work, Chang and Sun calculated the applied impact force by using an experimental Green's function and time-domain signal deconvolution [33]. The reconstructed force was identified independent of the location of the sensors on a composite beam structure. In both cases, the position of the impact was assumed to be known.

The deconvolution technique is also easily implemented in the frequency-domain for conducting force identification due to the ease of performing the deconvolution calculation since the convolution integral in the time-domain corresponds to a simple multiplication operation in the frequency-domain. In other work of Doyle, a frequency-domain deconvolution method was developed and used to experimentally determine contact laws [32]. The impact force was estimated by using analytical relationship between contact force and the strain response of structure. In order to improve the quality of the reconstructed force, signal processing techniques were applied on the strain response to avoiding the wrap-around problem [34, 35, 36].

Similar to the force identification methods, indirect methods of identification of the impact location have been studied extensively due to limitations in the direct identification of the impact location [26, 32, 37, 38, 39]. Methods for the localization of impacts can be classified into two main categories. The first type of method uses wave propagation speed and arrival time to determine impact location [40, 41, 42, 43, 44]. Methods in the first category take advantage of the wave speed and the recorded time for the traveling waves to reach

the sensors in order to calculate the position of the impact force. Gaul and Hurlebaus developed a method based on the arrival times of waves at various frequencies [40]. The location of the impact was identified by solving a nonlinear equation extracted from the speed of the traveling waves. The second type of localization of impact force is performed by minimizing an error function which is defined based on the impact force and the system response [45, 46, 47]. The system response can be obtained from a system model or transfer function which is derived analytically, numerically, or experimentally [48].

Additionally, it is possible for the two methods to be used simultaneously to accurately locate the impact force. In the recent work of Liang *et al.*, elements of the two methods were combined to create a distributed coordination algorithm for locating the impact force with greater computational efficiency [49]. However, further studies are required in order to fully explore the effectiveness of this approach.

2.3 Overview

In the section 3, the key elements of the two techniques for (i) modeling nonlinear wave propagation and (ii) performing force identification are presented. The performance of these methods is demonstrated in section 4. The main conclusions of this work and the direction of future work are presented in section 5. The material presented in this report constitutes the main advances which resulted from this work. For full details, refer to the publication produced through this work [50, 51, 52, 53, 54, 55, 56, 57, 58, 59, 60, 61, 62, 63, 64, 65].

3 Methodology

In this section, the methods developed in this work are presented. First, the Alternating Wavelet-Time Finite Element Method (AWT-FEM) is presented. Then, the force identification and force localization methods are presented.

3.1 Modeling Nonlinear Wave Propagation

A specific wavelet transform is described in the first subsection. The spectral finite element method formulation in the wavelet-domain is discussed in the second section. The procedure of AWT-FEM is described in the third subsection. Its applications to an elementary rod model with a material nonlinearity, an Euler-Bernoulli beam model with a geometric nonlinearity, and a conventional plate model with a weak geometric nonlinearity are derived in the last

subsection.

3.1.1 Spectrally-Uncoupled Wavelet Transform

The general governing differential wave equation of a nonlinear structure is given as [25]

$$\mathcal{L}\mathbf{u}(\mathbf{x},t) + \mathcal{M}\ddot{\mathbf{u}}(\mathbf{x},t) + \mathcal{N}\dot{\mathbf{u}}(\mathbf{x},t) + \mathbf{f}(\mathbf{u},\mathbf{x},t) = \mathbf{p}(\mathbf{x},t), \tag{1}$$

where $\mathcal{L}$ is the linear differential operator with respect to the spatial coordinate vector $\mathbf{x}$, the over-dot represents a derivative with respect to time t, $\mathcal{M}$ is the inertial operator, $\mathcal{N}$ is the damping operator, $\mathbf{u}(\mathbf{x},t)$ is the displacement field vector, $\mathbf{p}(\mathbf{x},t)$ is the external load vector, and $\mathbf{f}(\mathbf{x},t)$ is the nonlinear term vector.

A single-scale wavelet Galerkin's method using a Daubechies wavelet is applied to transform Eqn. (1) into a set of spectrally-uncoupled partial differential equations (PDEs). Details of this method and its application to a 1D linear wave equation can be found in [12, 20, 66]. Here, the application of this method to the general nonlinear wave equation in Eqn. (1) is briefly described in the following three steps.

Step 1:

A new variable $\tau = t/\Delta t$ is introduced. In the following derivation, τ is regarded as a continuous variable since integration with respect to τ will be performed.

$\mathbf{u}(\mathbf{x},t)$ is represented in an expansion form by translating the wavelet scaling function $\varphi(\tau)$.

$$\mathbf{u}(\mathbf{x},t) = \mathbf{u}(\mathbf{x},\tau) = \sum_k \mathbf{u}_k(\mathbf{x})\varphi(\tau - k), \quad k \in \mathbf{Z}, \tag{2}$$

where $\mathbf{u}_k(\mathbf{x})$ (referred as $\mathbf{u}_k$ hereafter) is the approximation coefficient of $\mathbf{u}(\mathbf{x},t)$ at an associated point k, $\mathbf{Z}$ is the set of integers.. By utilizing the orthogonality of the scaling function, the approximation coefficient $\mathbf{u}_k$ is obtained as

$$\mathbf{u}_k = \Delta t \int \mathbf{u}(\mathbf{x},\tau)\varphi(\tau - k)d\tau. \tag{3}$$

The scaling function $\varphi(t)$ is defined on the finest scale (the sampling scale). Hence, the integer k presents a shifting along the sampled time axis for k sample points. It is comparable to the frequency component at a given frequency in the Fourier expansion, in the sense that both the expansion in Eqn. (2) and

Fourier expansion expand the original function by a class of basis function indexed by a variable. The difference here is the index k indicates a shifting in time but the corresponding variable in Fourier expansion represents a refinement of frequency. The physical meaning of k indicates that the expansion in Eqn. (2) is in nature a shifting tool for a time integration technique. The index k is referred as "wavelet point" to distinguish the time series index τ before the expansion. Similarly, the nonlinear term $\mathbf{f}(\mathbf{x}, t)$ and the loading term $\mathbf{p}(\mathbf{x}, t)$ are expanded by $\mathbf{f}_k$ and $\mathbf{p}_k$ as follows.

$$\mathbf{f}(\mathbf{x}, t) = \sum_k \mathbf{f}_k \varphi(\tau - k), \quad k \in \mathbf{Z}, \tag{4}$$

$$\mathbf{p}(\mathbf{x}, t) = \sum_k \mathbf{p}_k \varphi(\tau - k), \quad k \in \mathbf{Z}. \tag{5}$$

The above expansions are substituted into Eqn. (1). By multiplying the resulting equation by the scaling function $\varphi(\tau - j)$ and integrating it over time, the following set of equations are obtained.

$$\begin{aligned} \mathcal{L}\mathbf{u}_j + \int \frac{\mathcal{M}}{\Delta t^2} \sum_k \mathbf{u}_k \ddot{\varphi}(\tau - k)\varphi(\tau - j)d\tau + \\ \int \frac{\mathcal{N}}{\Delta t} \sum_k \mathbf{u}_k \dot{\varphi}(\tau - k)\varphi(\tau - j)d\tau + \mathbf{f}_j \;\; = \;\; \mathbf{p}_j, \; j = 0, 1, \ldots, n-1, \end{aligned} \tag{6}$$

where $\mathbf{f}(\mathbf{x}, t)$, $\mathbf{p}(\mathbf{x}, t)$, and the $\mathbf{u}(\mathbf{x}, t)$ after the linear differential operator $\mathcal{L}$ are transformed into their corresponding approximation coefficients $\mathbf{f}_j$, $\mathbf{p}_j$, and $\mathbf{u}_j$ due to the orthogonality of the wavelet scaling function. For the time derivatives of $\mathbf{u}(\mathbf{x}, \tau)$, the two integrals associated with $\mathcal{M}$ and $\mathcal{N}$ in Eqn. (6) are evaluated in the form of connection coefficients for compactly supported wavelets [66], as defined in Eqn. (7) and (8). The index j represents a given wavelet point. Similar to the definition of k, it originally indicates a shifting along the time axis.

$$\Omega^1_{j-k} = \int \dot{\varphi}(\tau - k)\varphi(\tau - j)d\tau, \tag{7}$$

$$\Omega^2_{j-k} = \int \ddot{\varphi}(\tau - k)\varphi(\tau - j)d\tau. \tag{8}$$

For a multidimensional problem, $\mathbf{u} = [u, v, w]^T$ and $\mathbf{u}_j = [u_j, v_j, w_j]^T$, a complete matrix form of Eqn. (6) with respect to the three dimensions and the wavelet point j is cumbersome. The couplings between different dimensions (x, y, z) are assumed to be represented in the nonlinear term $\mathbf{f_j}$. Since $\mathbf{f_j}$ will

be treated as an equivalent nodal force term without explicitly evaluating it, and only its nodal values will be used in the numerical procedure to solve the equation, Eqn. (6) can be regarded as decoupled with respect to dimensions. The coupling in Eqn. (6) is with respect to the index j and is captured in the matrix $\mathbf{\Omega}$. Hence, Eqn. (6) describes a set of spectrally coupled PDEs with respect to j, and has to be solved for each wavelet point (translation along time axis) j.

Step 2:

Next, a wavelet extrapolation technique [20] is adopted to address the time boundaries. Specific treatments of periodic and non-periodic time boundaries for linear wave equations can be found in [12]. It uses a polynomial of order $N/2-1$ to extrapolate the values at the boundaries from the known coefficients near the boundaries. The connection coefficient matrix $\mathbf{\Omega}$ becomes a $n \times n$ matrix $\mathbf{\Lambda}$, which is a version with non-periodic time boundaries. The result of this process is arranged into three decoupled matrix forms with respect to the three dimensions, each of which will be further decoupled with respect to the spectral index j in the next step.

Step 3:

A standard eigenvalue analysis is performed to uncouple the matrix form of Eqn. (6) with respect to j. The eigenvalue and the $n \times n$ eigenvector matrix of the $n \times n$ connection coefficient matrix Λ are $\lambda_j,\ j = 0, 1, \cdots, n-1$ and Φ, respectively. After each dimension is spectrally uncoupled, the result can be organized as

$$\mathcal{L}\hat{\mathbf{u}}_j + \left(\mathcal{M}\lambda_j^2 + \mathcal{N}\lambda_j\right)\hat{\mathbf{u}}_j + \hat{\mathbf{f}}_j = \hat{\mathbf{p}}_j, \quad j = 0, 1, \ldots, n-1, \tag{9}$$

where the eigenvalue λ_j can be treated as a pseudo-frequency and is related to the physical angular frequency ω_j in the Fourier transform through $\lambda_j = i\omega_j$, and

$$\begin{aligned}
\hat{\mathbf{u}}_j &= \left[\hat{u}_j, \hat{v}_j, \hat{w}_j\right]^T, \\
\hat{\mathbf{f}}_j &= \left[\hat{F}_{uj}, \hat{F}_{vj}, \hat{F}_{wj}\right]^T, \\
\hat{\mathbf{p}}_j &= \left[\hat{P}_{uj}, \hat{P}_{vj}, \hat{P}_{wj}\right]^T, \\
\{\hat{u}_j\} &= \Phi^{-1}\{u_j\}, \\
\{\hat{v}_j\} &= \Phi^{-1}\{v_j\}, \\
\{\hat{w}_j\} &= \Phi^{-1}\{w_j\},
\end{aligned}$$

$$
\begin{aligned}
\left\{\hat{F}_{uj}\right\} &= \Phi^{-1}\left\{F_{uj}\right\}, \\
\left\{\hat{F}_{vj}\right\} &= \Phi^{-1}\left\{F_{vj}\right\}, \\
\left\{\hat{F}_{wj}\right\} &= \Phi^{-1}\left\{F_{wj}\right\}, \\
\left\{\hat{P}_{uj}\right\} &= \Phi^{-1}\left\{P_{uj}\right\}, \\
\left\{\hat{P}_{vj}\right\} &= \Phi^{-1}\left\{P_{vj}\right\}, \\
\left\{\hat{P}_{wj}\right\} &= \Phi^{-1}\left\{P_{wj}\right\}, \qquad (10)
\end{aligned}
$$

where the bracket represents a vector formation with respect to j.

These three steps define a special single-scale wavelet transform to reduce a temporal problem into a set of spectrally-uncoupled PDEs. This procedure involves several wavelet-based numerical techniques [20, 66], an eigenvalue analysis, and an inverse calculation of matrices. However, it is worth noting that this procedure is independent of the system to be studied and must only be performed once for a given wavelet scaling function $\varphi(t)$ and length of time window n. The resulting eigenvalues λ_j, eigenvector matrix Φ, and the inverse of Φ can then be calculated and stored for future use. The scaling function is defined at the sampling rate of the signal, which is also the finest scale achievable for a given set of data. In the above wavelet transform procedure, the approximation coefficient of a given signal is first obtained by using a numerical applying of Eqn. (3). The vector of approximation coefficients, which has the same length as the original signal, is multiplied by the inverse of the eigenvector matrix Φ in order to obtain the corresponding values in the defined wavelet-domain. The inverse transform is then performed by multiplication by the eigenvector matrix Φ to obtain the approximation coefficients in the time-domain. The signal is recovered by finally using Eqn. (2).

3.1.2 Spectral Finite Element Method Formulation

Various methods are available to solve the linear version of Eqn. (9). In [22, 23], the SEM is chosen to solve general linear 2D and 3D problems in the wavelet-domain. In this study, the research focus is to develop a numerical technique for structures that can be modeled with rod, beam, and plate elements. Utilizing the analytical wave solutions of those models may greatly improve the computational efficiency and alleviate potential convergence issues with the iterative approach that will be constructed to address nonlinearities.

The linear homogeneous wave equation is obtained by removing the non-

linear term and external force term in Eqn. (9).

$$\mathcal{L}\hat{\mathbf{u}}_j + \left(\mathcal{M}\lambda_j^2 + \mathcal{N}\lambda_j\right)\hat{\mathbf{u}}_j = 0, \quad j = 0, 1, \ldots, n-1. \tag{11}$$

For 1D problems, $\mathbf{x} = x$ and Eqn. (9) is a set of nonlinear ODEs. Exact solutions to Eqn. (11) for rod and beam structures are well-established [7]. In linear SFEM, those exact solutions are directly employed to solve for the response at a given location x and only one element is needed for the formulation. In this nonlinear derivation, the exact linear solutions are adopted as the shape functions in a standard finite element framework in the wavelet-domain. The spectral displacement vector $\hat{\mathbf{u}}_j$ is expressed as

$$\hat{\mathbf{u}}_j = \mathbf{N}(x; \lambda_j)\mathbf{q}_j, \tag{12}$$

where $\mathbf{N}(x; \lambda_j)$ (referred as $\mathbf{N}$ hereafter) is the spectral shape functions based on the exact linear wave solutions, and $\mathbf{q}_j$ is the spectral nodal displacement vector at the pseudo-frequency λ_j or wavelet point j. By following a standard Galerkin's method, the nonlinear ODE in Eqn. (9) becomes the following matrix form

$$\mathbf{K}(\lambda_j)\mathbf{q}_j = \mathbf{q_E} + \mathbf{q_N}, \tag{13}$$

where

$$\begin{aligned}
\mathbf{K}(\lambda_j) &= \int \left(\mathbf{A}(\mathbf{N}, \mathbf{N}) + \mathbf{N}^T\left(\mathcal{M}\lambda_j^2 + \mathcal{N}\lambda_j\right)\mathbf{N}\right) dx, \\
\mathbf{q_E} &= \int \mathbf{N}^T \mathbf{p}_j dx, \\
\mathbf{q_N} &= \int \mathbf{N}^T \mathbf{f}_j dx.
\end{aligned} \tag{14}$$

The spectrally formulated dynamic stiffness matrix is represented by $\mathbf{K}(\lambda_j)$, $\mathbf{A}(\mathbf{N}, \mathbf{N})$ is the function resulting from integration by parts [19], $\mathbf{q_E}$ is the equivalent nodal force term for the distributive external load, and $\mathbf{q_N}$ is the equivalent nodal force term for the nonlinear term. It is worth noting that the process to derive Eqn. (13) may involve several steps of iteration by parts, so the sign on the right-hand side may change depends on the explicit form of $\mathcal{L}$. The expression in Eqn. (13) is for the purpose of a general and concise representation.

For a 2D problem, $\mathbf{x} = \{x, y\}$ and Eqn. (9) is a set of nonlinear PDEs. The wavelet transform is performed again on Eqn. (9) with respect to one of the spatial coordinate y. After that, Eqn. (9) is reduced to a set of ODEs and the model is simplified into a 1D problem. A similar spectral finite element

method formulation as above can be performed to obtain a matrix form as in Eqn. (13). An example of this spatial reduction process for a plate model is provided at the end of this section.

3.1.3 General Procedure of the AWT-FEM

Based on the spectrally-uncoupled wavelet transform and the spectral finite element method formulation in the wavelet-domain, an alternating wavelet-time framework is constructed to iteratively simulate nonlinear elastic wave propagation responses. A flowchart of the AWT-FEM is presented in Fig. 1. The initial state is obtained from the linear model by setting the nonlinear term $\mathbf{f}(\mathbf{u}, \mathbf{x}, t)$ in Eqn. (1) equal to zero. The $\mathbf{f}(\mathbf{x}, t)$ is written as $\mathbf{f}(\mathbf{u}, \mathbf{x}, t)$ to indicate that the value of the nonlinear force term is directly determined by the current value of $\mathbf{u}$. At each iteration, the nodal values of the nonlinear term $\mathbf{f}(\mathbf{u}, \mathbf{x}, t)$ are calculated from the current states in the time-domain. The result and the nodal values of external force $\mathbf{p}(\mathbf{x}, t)$ are transformed into the wavelet-domain through the spectrally-uncoupled wavelet transform. At each pseudo-frequency or wavelet point, a spectral finite element method formulation is constructed based on Eqn. (13) to obtain nodal values of $\hat{\mathbf{u}}_j$. Nodal values of the derivatives of $\hat{\mathbf{u}}_j$ with respect to $\mathbf{x}$ are easily calculated based on Eqn. (12). Since Eqn. (9) is uncoupled with respect to j, the above calculation is performed in parallel at each wavelet point. The nodal information is then transformed back to the time-domain via the inverse wavelet transform. New values of the nonlinear term $\mathbf{f}(\mathbf{x}, t)$ are calculated for use in the next iteration. The process is continued until the predefined error measure defined in Eqn. (15) is less than a prescribed tolerance.

The number of wavelet point is determined by the length of the signal. The higher the sampling rate and the longer the signal length, the better accuracy of the wavelet transform and a better performance of the AWT-FEM, since Eqn. (2) and (3) are implemented through numerical integration in the program. In most of the applications, the signal is collected through experiments or predefined as inputs. Hence, the length of the signal or the number of wavelet point is taken as fixed conditions in numerical simulation in this study.

$$\beta_i = \frac{1}{M} \sum_{m=1}^{M} \left\| \frac{\mathbf{f}_i(\mathbf{x}_0, t_m) - \mathbf{f}_{i-1}(\mathbf{x}_0, t_m)}{\mathbf{f}_i(\mathbf{x}_0, t_m)} \right\|, \tag{15}$$

where M is the length of the time history, $\mathbf{x}_0$ is the impacted location, and the subscript i represents the iteration number. The response at the impacted po-

sition has both the initial impulse profile and the interaction with the reflected wave from the boundary within a given time-window. It can reflect most of the accumulated nonlinear information in the wave propagation process. Hence, the impact position is chosen to define the error measure. Other point might also be used and the result will not be qualitatively different.

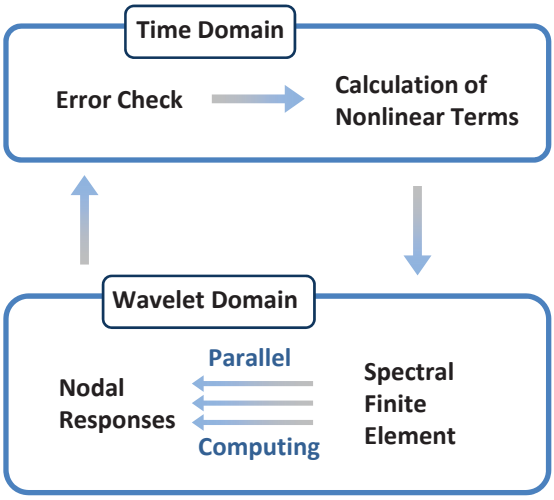

Figure 1: The flowchart for the AWT-FEM.

3.2 Applications to Structural Models

(1) Rod:

A rod model with a material nonlinearity is considered here. A general nonlinear stress-strain relationship with a high order strain term has been used in [8, 17, 67]. In the second order case, the nonlinear constitutive law becomes

$$\sigma = E(\epsilon + \alpha\epsilon^2), \tag{16}$$

where σ is the stress, ϵ is the strain, E is the elastic modulus, and α is the nonlinear coefficient. When $\alpha > 0$, the quadratic term exhibits a hardening effect on the constitutive curve. When $\alpha < 0$, a softening effect can be observed.

A linear strain-displacement relationship $\epsilon = du/dx$ is assumed. By using Hamilton's principle, the governing materially nonlinear homogeneous wave equation for a rod is obtained as

$$EAu'' - \rho A\ddot{u} + F(x,t) = 0, \tag{17}$$

where

$$F(x,t) = 2\alpha EAu'u'', \tag{18}$$

the cross sectional area is represented by A, ρ is the density, u is the axial displacement, the prime represents a derivative with respect to the spatial coordinate x, and $F(x,t)$ is the nonlinear term.

By using the spectrally-uncoupled wavelet transform previously described, the governing equation of motion in the wavelet-domain is obtained as

$$EA\hat{u}_j'' - \rho A\lambda_j^2\hat{u}_j + \hat{F}_j = 0, \quad j = 0, 1, \ldots, n-1. \tag{19}$$

The expression of the spectrally-dependent shape function $\mathbf{N_R}$ for a rod model can be found in Eqn. (3.36) in [19]. It is a 1×2 vector with components as functions of x and ω. The angular frequency ω associated with the frequency-domain implementation in the references must be replaced by $\omega = -i\lambda_j$ for this wavelet-domain method, which is indicated by comparing the Eqn (11) in the wavelet-domain with Eqn (3.4) in [19] in the frequency-domain. By substituting it into Eqn. (14), the dynamic stiffness matrix $\mathbf{K}$ and the equivalent nodal nonlinear force term $\mathbf{q_N}$ become

$$\begin{aligned} \mathbf{K} &= \int EA\mathbf{N}_\mathbf{R}'^T\mathbf{N}_\mathbf{R}'dx + \lambda_j^2\int \rho A\mathbf{N}_\mathbf{R}^T\mathbf{N}_\mathbf{R}dx, \\ \mathbf{q_N} &= \int \mathbf{N}_\mathbf{R}^T\hat{F}_j dx. \end{aligned} \tag{20}$$

(2) Beam:

A beam model with a geometric nonlinearity is considered here. The strain is assumed to be small and the rotation is expected to be moderately large. The *von Kármán* strain [9] is defined to represent the nonlinear strain-displacement relationship. The constitutive relationship is assumed to be linear. By using Hamilton's principle, the governing geometrically nonlinear homogeneous wave equations for a beam are obtained as

$$EAu'' - \rho A\ddot{u} + F_R(x,t) = 0, \tag{21}$$

$$EIw'''' + \rho A\ddot{w} - F_B(x,t) = 0, \tag{22}$$

where

$$F_R(x,t) = EAw'w'', \tag{23}$$

$$F_B(x,t) = EAw''\left(u' + \frac{1}{2}(w')^2\right), \tag{24}$$

the axial displacement is represented by u, w is the transverse displacement, I is the second moment of inertia, $F_R(x,t)$ is the axial nonlinear force term, and $F_B(x,t)$ is the transverse nonlinear force term. The definitions of E and A are same as those for the rod model.

By using the spectrally-uncoupled wavelet transform developed in the first subsection, the governing equations in the wavelet-domain is obtained as

$$EA\hat{u}_j'' - \rho A\lambda_j^2\hat{u}_j + \hat{F}_{Rj}(x) = 0, \tag{25}$$

$$EI\hat{w}_j'''' + \rho A\lambda_j^2\hat{w}_j - \hat{F}_{Bj}(x) = 0, \quad j = 0, 1, \ldots, n-1. \tag{26}$$

The expression of the spectrally-dependent axial shape functions $\mathbf{N_R}$ and transverse shape functions $\mathbf{N_B}$ can be found in Eqn. (3.36) and Eqn. (3.56) in [19]. The transverse shape function $\mathbf{N_B}$ is a 1×4 vector with components as functions of x and ω. As was done for rod structures, the angular frequency ω in the references must be replaced by $\omega = -i\lambda_j$. By organizing Eqn. (25) and Eqn. (26) into a matrix form and performing the spectral finite element formulation, the dynamic stiffness matrix $\mathbf{K}$ becomes

$$\mathbf{K} = \begin{bmatrix} K_{R11} & 0 & 0 & K_{R12} & 0 & 0 \\ 0 & K_{B11} & K_{B12} & 0 & K_{B13} & K_{B14} \\ 0 & K_{B21} & K_{B22} & 0 & K_{B23} & K_{B24} \\ K_{R21} & 0 & 0 & K_{R22} & 0 & 0 \\ 0 & K_{B31} & K_{B32} & 0 & K_{B33} & K_{B34} \\ 0 & K_{B41} & K_{B42} & 0 & K_{B43} & K_{B44} \end{bmatrix}, \tag{27}$$

where K_{Rij} and K_{Bij} are components of $\mathbf{K_R}$ and $\mathbf{K_B}$, respectively.

$$\mathbf{K_R} = \int EA\mathbf{N_R'}^T\mathbf{N_R'}dx + \lambda_j^2\int \rho A\mathbf{N_R}^T\mathbf{N_R}dx, \tag{28}$$

$$\mathbf{K_B} = \int EI\mathbf{N_B''}^T\mathbf{N_B''}dx + \lambda_j^2\int \rho A\mathbf{N_B}^T\mathbf{N_B}dx. \tag{29}$$

The dynamic stiffness matrix $\mathbf{K}$ is decoupled between axial and transverse motions. The equivalent nodal nonlinear force term $\mathbf{q_N}$ becomes

$$\mathbf{q_N} = \begin{Bmatrix} \int N_{R1}\hat{F}_{Rj}dx \\ \int N_{B1}\hat{F}_{Bj}dx \\ \int N_{B2}\hat{F}_{Bj}dx \\ \int N_{R2}\hat{F}_{Rj}dx \\ \int N_{B3}\hat{F}_{Bj}dx \\ \int N_{B4}\hat{F}_{Bj}dx \end{Bmatrix}, \tag{30}$$

where the terms N_{Ri} and N_{Bi} are elements of $\mathbf{N_R}$ and $\mathbf{N_B}$, respectively. The general spectral nodal displacement vector is defined as $\mathbf{q}_j = \left[\hat{u}_1\ \hat{w}_1\ \hat{\theta}_1\ \hat{u}_2\ \hat{w}_2\ \hat{\theta}_2\right]^T$, where $\hat{\theta}$ is the rotation angle in the wavelet-domain.

(3) Plate:

A plate model with a geometric nonlinearity is considered here. In [9], the classic and first-order plate theory with the *von Kármán* strain is chosen to derive the governing equation of motion. The results are three coupled nonlinear equations in the three spatial dimensions with respect to two in-plane displacements u, v, and one out of plane displacement w. The equation in the direction perpendicular to the plane can be written into the form of *von Kármán* equation [68] as

$$D\nabla^2\nabla^2 w(x,y,t) + \rho h\ddot{w}(x,y,t) = F(x,y,t), \tag{31}$$

where $\nabla^2 = \partial^2/\partial x^2 + \partial^2/\partial y^2$ is the Laplace operator, h is the thickness of the thin plate, w is the transverse displacement, $D = Eh^3/(12(1-\nu^2))$ is the flexural rigidity, and ν is the Poisson's ratio. Other parameters are defined as same as those in the rod model. The nonlinear term $F(x,y,t)$ is

$$F(x,y,t) = N_{xx}\frac{\partial^2 w}{\partial x^2} + N_{yy}\frac{\partial^2 w}{\partial y^2} + 2N_{xy}\frac{\partial^2 w}{\partial x \partial y}, \tag{32}$$

where N_{xx}, N_{yy}, and N_{xy} are resultant membrane forces defined as

$$N_{xx} = \int_{-h/2}^{h/2} \sigma_{xx} dz, \quad N_{yy} = \int_{-h/2}^{h/2} \sigma_{yy} dz, \quad N_{xy} = \int_{-h/2}^{h/2} \sigma_{xy} dz, \tag{33}$$

where the expressions of stresses σ_{xx}, σ_{yy}, and σ_{zz} can be calculated from the strains defined in Eqn.(6.2.5) in [9].

Equation (32) indicates that the nonlinear term is a function of three unknowns u, v, and w, which correspond to displacement along x, y, and z axis. Two assumptions are made here to further simplify the model. First, it is assumed that the plate is only subject to transverse loading. Second, it is assumed that there are either no axial constraints on the boundaries or the plate is large enough so that the propagating wave will not reach the boundaries within the time window. In this weak geometric nonlinear case, the in-plane displacement u and v are very small and can be assumed to be zero in Eqn. (31) and Eqn. (32).

By using the spectrally-uncoupled wavelet transform, Eqn. (31) is transformed into the wavelet-domain as

$$D\nabla^2\nabla^2 \hat{w}_j(x,y) + \rho h\lambda_j^2 \hat{w}_j(x,y) = \hat{F}_j(x,y) \quad j = 0, 1, \ldots, n-1. \tag{34}$$

The spectrally-uncoupled wavelet transform is applied again with respect to one of the spatial dimension y and Eqn. (34) is reduced to a 1D problem as

$$D\left(\frac{d^4\tilde{w}_{ij}}{dx^4}+2\beta_i^2\frac{d^2\tilde{w}_{ij}}{dx^2}+\beta_i^4\tilde{w}_{ij}\right)+\rho h\lambda_j^2\tilde{w}_{ij}=\tilde{F}_{ij}. \quad i,j=0,1,\ldots,n-1, \tag{35}$$

where β_i is a pseudo spatial frequency. For more information about this spatially reduction process, refer to [21] where a similar example for a linear plate model is presented (Chapter 7.3, Eqn. (7.34) to Eqn. (7.37)).

Equation (35) is analogous to a beam equation. By setting $\tilde{F}_{ij}$ as zero, Eqn. (35) becomes a linear homogeneous wave equation. The exact solution is assumed to be $\tilde{w}_{ij}=ce^{-ikx}$ and substituted into the linear homogeneous wave equation. Four values of the wavenumber $k(\beta_i,\lambda_j)$ are obtained through an eigenvalue analysis. The spectrally-dependent shape function $\mathbf{N_B}$ is defined in Eqn. (3.56) in [19]. The wavenumber k in the references must be replaced by the new calculated values. The dynamic stiffness matrix $\mathbf{K}$ and the equivalent nodal nonlinear force term $\mathbf{q_N}$ are derived as

$$\begin{aligned}\mathbf{K} &= \int D\mathbf{N}_\mathbf{B}''^T\mathbf{N}_\mathbf{B}''dx-\int 2D\beta_i^2\mathbf{N}_\mathbf{B}'^T\mathbf{N}_\mathbf{B}'dx+\\ &\quad \int(D\beta_i^4+\rho h\lambda_j^2)\mathbf{N}_\mathbf{B}^T\mathbf{N}_\mathbf{B}dx \qquad (36)\\ \mathbf{q_N} &= \int \mathbf{N}_\mathbf{B}^T\tilde{F}_{ij}dx, \qquad (37)\end{aligned}$$

where explicit expressions of integral terms can be referred to the ones in the beam model.

3.3 Impact Force Identification

In the impact force identification method presented in this section, the dynamic stiffness matrix is prepared for the structure and multiplied by the displacement and slope information in order to calculate the identified force. However, incomplete deflection and slope data results in errors in the calculated force information. Mechanical wave propagation starts immediately after the impact force is applied and it moves out from this location until it reaches the ends of the structure and is reflected. In order to capture the complete wave propagation data across the entire beam structure, accelerometers must be mounted along the entire length of the beam, including at the ends. However, mounting accelerometers at the ends of the structure and densely along the length is not always practical. Therefore, in this work a force identification

method is presented that utilizes the data of the propagating wave recorded by using accelerometers located near the location of the impact. Although the exact location of the impact is unknown, it is assumed that the general area in which the impact occurs is known.

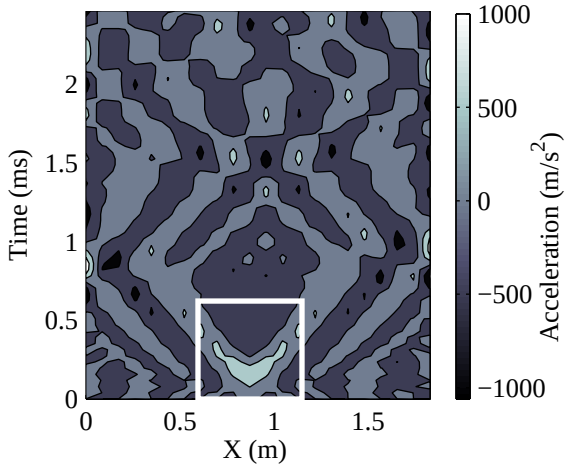

Figure 2: Simulated wave propagation (acceleration data) in a free-free beam. The boxed area corresponds to data which is selected for analysis. This area corresponds to only a section of the structure and does not include reflections.

The simulation acceleration data of wave propagation through the beam structure is illustrated in Fig. 2. The figure illustrates the variation of acceleration at each location of the beam through time. This response is used in order to identify the impact force. After the impact occurs, mechanical waves travel through the beam structure and reflect when they reach the ends. The reflections and dispersion in beam structures increase the difficulty of performing successful force identification, especially if it is not possible to mount sensors at the ends of the structure. In this force identification method, the impact force is calculated by using a SFEM model and a subset of the response data. This subset of the displacement and slope data corresponds to a reduction in both the spatial and temporal dimensions around the location where the propagated wave originated, as illustrated by the box in Fig. 2. Note that acceleration data is presented in this figure. This subset of data chosen for the identification procedure is selected so that it does not contain reflections. The data subset is used with a beam segment model to calculate the desired force information.

A flowchart of the force identification procedure is presented in Fig. 3. The

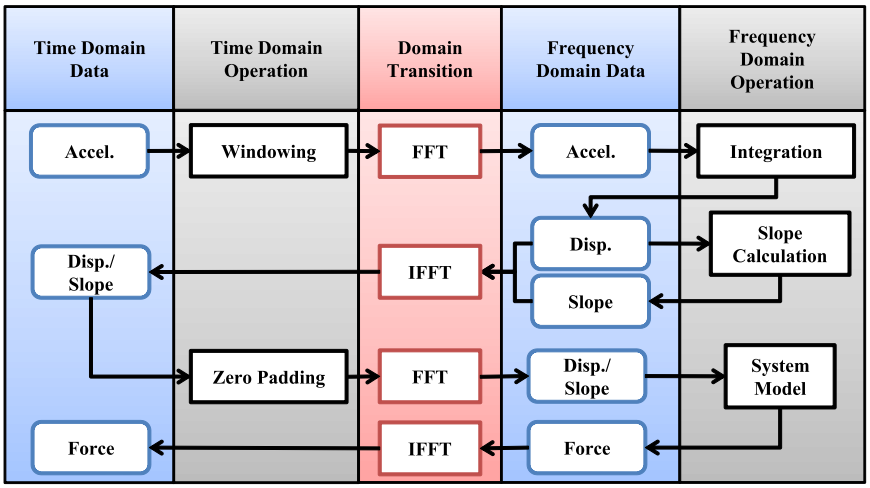

Figure 3: Flowchart illustrating the main steps of the force identification scheme.

acceleration data from the structure is transformed into the frequency-domain by using the fast Fourier transform (FFT) and is integrated twice to obtain displacement. The slope information required for the identification process is calculated by using a shape function-based method. Zero-padding is applied to the response data in order to address the FFT's assumption of periodicity. The dynamic stiffness matrix of the SFEM model for a segment of the beam is used to calculate the force information in the frequency-domain. Detailed descriptions of each step are presented in the following subsections.

3.3.1 Time-Domain Signal Conditioning

The force identification procedure uses the propagating wave data immediately after the impact to identify the impulsive force. A simple algorithm is applied to the acceleration data in order to identify the general area of the beam where the impact occurred. The geometry and material properties of the structure are used to approximate the length of time after the impact when reflections are expected to occur. Exponential windowing is applied to the complete time series of the experimental acceleration data in order to reduce frequency-domain leakage in the response [69]. Exponential windowing causes the acceleration to decay to zero at the end of the full data set and ensures periodicity in the response. Since only a small portion of the data immediately after the impact is used, this windowing has a negligible effect on that data

and subsequently the identified force information.

Since the FFT algorithm assumes periodicity, it can result in wrap-around issues. Zero padding is later applied in order to address this concern. Zero padding has been shown to significantly improve the quality of force information identified by using frequency-domain methods [32].

3.3.2 Deflection Information

Deflection information is required for the force identification procedure. The deflections of the nodes are calculated from the acceleration data. The integration is performed in the frequency-domain in order to improve accuracy and ensure compatibility with the frequency-domain representation of the system [70]. The integration is performed by dividing the frequency-domain acceleration data by the imaginary form of the frequency. For the zero frequency, a DC value is used for the integration which is the summation of the acceleration values in the frequency-domain [70]. However, this has been shown to result in drift in the time history of displacement data. Fortunately, the small portion of the displacement data right after the impact which is used for the force identification problem is negligibly influenced by the drift.

3.3.3 Slope Calculation

The acceleration data only provides information regarding the one-dimensional translational motion at discrete points along the structure but application of the force identification procedure to a beam structure requires both deflection and slope information. Therefore, it is necessary to calculate the corresponding slope response at each location. This is accomplished by taking advantage of the kinematics of the beam structure. In the slope calculation process, the slope information of the beam structure is obtained by using the shape function of the SFEM beam model of the structure. This technique is precise when the kinematics of the structure is known. In order to calculate the slopes by using shape functions, the beam structure is meshed with four-node beam elements that provide C^0 continuity.

The slope calculation procedure is performed in the frequency-domain by using deflection data at each node. The deflection coefficients, $\hat{A}$, $\hat{B}$, $\hat{C}$, and $\hat{D}$, of each four-node beam element are calculated by substituting the deflection values at the four nodes for the specified range of frequencies into the deflection equation and solving for the deflection coefficients. Slope information is obtained by using the analytical derivative of the shape functions.

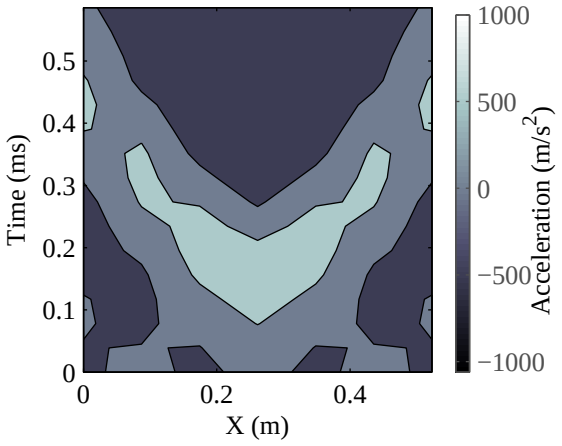

Figure 4: Simulated mechanical wave propagation (acceleration data) using segment model which includes two throw-off elements.

3.3.4 SFEM Model for Force Identification

The SFEM model used in the force identification process represents a segment of the beam structure. The implementation of the force identification method presented here utilizes the response data from the five accelerometer positions in the vicinity of the impact force. The spectral finite element model is constructed by using a throw-off element at each end of the segment. For these conditions, the frequency-domain dynamic stiffness matrix is prepared to relate the displacement and slope information to the corresponding force and moment information for the beam segment. Although this model differs considerably from the full structure model, a response predicted by the segment model with the same impact force previously considered, shown in Fig. 4, matches perfectly with the local response behavior of the full structure, identified by the box in Fig. 2.

Due to the nature of SFEM, this force identification method calculates nodal forces. For conditions where the location of the applied load and the accelerometer are collocated, the force identification process does not require any additional steps in order to obtain the identified force information. However, for cases where the impact is applied between two accelerometers, point forces are calculated at the neighboring nodes when the force identification procedure is applied. The summation of the two force time histories produces the identified force when certain conditions are satisfied. These conditions and the justification for this process is discussed in section 3.4 where the location

identification process is presented. This approach allows for the impact force information to be efficiently identified independent of the exact location of the impact.

3.3.5 Numerical Implementation and Parametric Study

The force identification procedure is first applied to the deflection and slope data from the numerical simulations. This eliminates the potential error introduced by the deflection and slope calculations and allows for the study to focus on the influence of other conditions on the performance of the force identification method. The theoretical test structure used to numerically study the performance of the force identification method is an 18 ft (5.49 m) long Aluminum beam with a square cross-section and width of 1 in (25.4 mm). Density and Young's modulus values of $\rho = 2700$ kg/m^3 and $E_Y = 75$ GPa are used and a damping coefficient value of $\eta = 10^4$ Ns/m^4 is identified to match the experimental response. The test structure is chosen for geometric simplicity in order to facilitate experimental verification.

In order to study the effects of various parameters on the performance of the force identification procedure, an ideal condition is defined. The theoretical test structure is studied with free-free boundary conditions. The full structure simulation is conducted by using a SFEM model with 66 evenly spaced nodes and a point impact force is applied. The time window for the numerical simulation is 2.56 s which allows for the propagating mechanical waves to fully dissipate for the complete structure model without throw-off elements. The force information calculated with the proposed method corresponds to the accelerometer locations which were included in the subset of data analyzed. For the ideal condition, the impact force is applied to a node in the middle of the structure in order to minimize the effect of the reflections on the accuracy of the identified force information. The duration of the impact is 0.4 ms, which can be realized experimentally.

The SFEM model and numerical simulations of the response of the structure are prepared and performed by using MATLAB. The proposed force identification method is also implemented and studied by using MATLAB and applied to the simulated response data to study the method. Both the simulation of the response data and the analysis of this data are performed by using SFEM-based approaches. This procedure is used since other simulation techniques, such as time-domain methods, have been found to display limitations with regard to high frequency performance [14]. For this reason, experimental response data is also used in order to validate the performance of the force identification method.

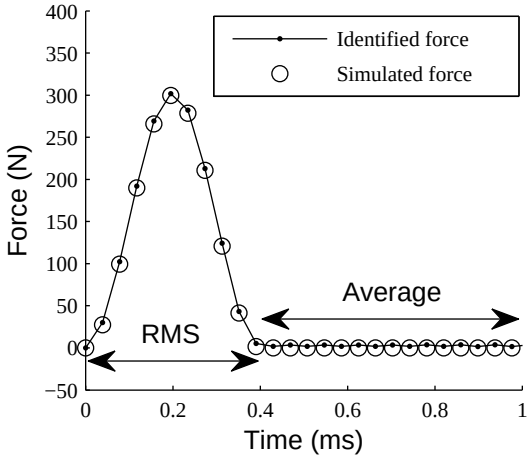

Figure 5: Force information calculated for the simulated response for an 18 ft (5.49 m) long beam. For this nominal case, there is strong agreement between the identified (connected points) and simulated (circles) force information.

For the ideal conditions, the point force is detected at the location of the impact, which is at node 33 at a position of 8.85 ft (2.70 m) from the reference end of the beam. The peak calculated forces at the other nodes within the subset of data analyzed have values less than 6 N ($< 2\%$), which are easily distinguished from the identified impact force. The force information identified from the simulated response, shown in Fig. 5, agrees very well with the simulated force. In order to quantify the accuracy of the force identification method, a Root Mean Square (RMS) error is calculated by comparing the identified force values to the values used in the simulation. The RMS error for impact force identification [27] provides quantitative information about the average error through the impact time history. The quantification of the error is performed by first separating the time series into two regions: the impulsive load and the remaining portion of the time history, as shown in Fig. 5. For the nominal case, the RMS error is 2.72 N during the impact and an average value of 2.46 N exists for the impact force considered over the remainder of the 1 ms presented. These errors are quite small when compared with the 300 N peak value of the impulsive load, less than 1 percent. The presence of error in the identified force information for the nominal case results from the use of the segment model and how it differs from the complete structure. However, the use of the segment model provides the means for the practical implementation of the force identification method.

The geometric and loading properties corresponding to the results presented in Fig. 5 provide nominal conditions for performing force characterization. Variations of these properties are studied in order to determine how they influence the ability of the force identification method to accurately calculate the applied impulsive load. This includes the effects of (i) varying the length of the structure, (ii) using calculated slope information instead of simulated slope information, (iii) varying the location of the applied force, (iv) varying the duration of the impulsive load, and (v) varying the length of the response data analyzed. During each part of the parametric study, the values of the parameters not currently being investigated are set to the values corresponding to the ideal conditions. The acceleration signals used in the numerical studies do not contain noise.

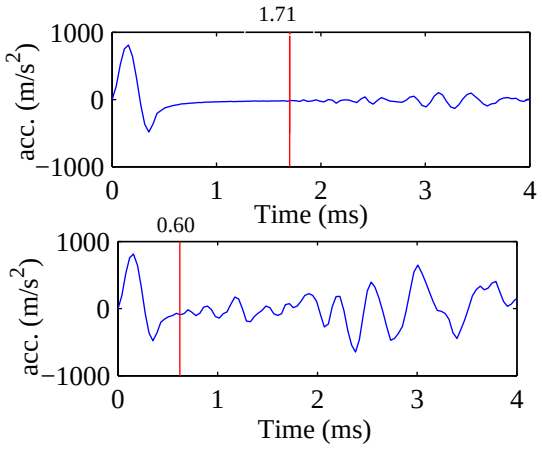

Figure 6: Acceleration response at a node near the center of the beam for (top) 18 ft (5.49 m) beam and (bottom) 6 ft (1.83 m) beam. Vertical lines identify when the reflection returns to the impact location.

(i) Structure Length

In order to study the influence of the length of the structure on the accuracy of the calculated force information, the force identification process is applied to response behavior simulated for a range of lengths from 0.5 ft (0.15 m) to 18 ft (5.49 m). In each case, the impact force is applied at a node in the middle of the structure. While the length of the structure is varied, all other conditions are maintained and the simulated displacement and slope information is used for the force calculation. The main effect of varying the length of the structure is to change the length of time before the reflected waves return the location

where the impact force was applied. This effect is illustrated in Fig. 6.

The vertical lines in Fig. 6 indicate the time when the reflection is observed in the acceleration data. For the nominal case with an 18 ft (5.49 m) long beam, the reflection is observed after 1.71 ms. When the beam length is reduced to 6 ft (1.83 m), reflections are observed after only 0.60 ms. Since the shorter length is one-third the initial length, it takes roughly 1/3 of the time before the reflected wave returns. This time depends on the length of the beam as well as the wave speed. Since wave propagation is dispersive in beam structures, the components of the mechanical waves at different frequencies travel with different speeds. The return of the reflected waves is identified by detecting oscillations in the response data after the initial wave.

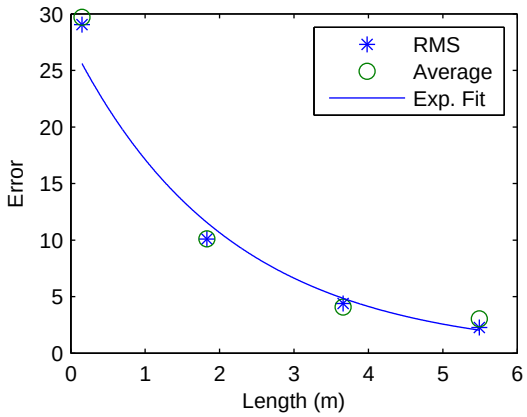

Figure 7: Force identification error with respect to the length of the structure. RMS error (*) during the impulsive load, average force (o) after the impulsive load, and a logarithmic curve (−) fit to the RMS error values are presented.

Error information is obtained by applying the force identification scheme to the response data simulated for beam structures of lengths within identified range. The RMS error values (*) obtained by comparing the simulated and identified force values during the impulsive force and the average identified force values (o) after the impulsive force are presented in Fig. 7. Examination of these error values reveal that as the length of the structure is decreased, the values of both error measures appear to increase along a logarithmic profile. This is confirmed by using a least squares approach to fit the RMS error values to a logarithmic curve: $Error = -7.55ln\,(L) + 14.67$ with $R^2 = 0.9999$. A similar logarithmic curve is also found to fit the trend of the values of the other error measure (not shown). In addition to displaying the same logarithmic

behavior, it can also be seen in Fig. 7 that the values of the two error measures are very close at all of the lengths considered. This suggests that the influence of structure length on the performance of the force identification method is not significantly affected by the magnitude of the force information. The increase in the error measure values which are observed for beam structures with shorter lengths is the result of the shorter amount of time before the reflected wave returns to the position on the structure where the force was applied. With less time before the reflections occur, the subset of data which can be used by the force identification method is reduced and greater deviation exists between the data and the behavior expected by the segment model.

(ii) Slope Calculation

The slope calculation method is tested by using deflection and slope data from numerical simulations. The slope information calculated from the simulated deflection data demonstrates excellent agreement with the simulated slope information. The maximum difference between the calculated and simulated slope data is between nine and ten orders of magnitude less than the values of the slope from the simulation.

The error introduced by including the slope calculation in the force identification procedure is determined to be negligible for the simulated response data. By using the shape function method to calculate the slope information, the error in the identified impulsive force does not change from the nominal case. However, noise in the response can cause the accuracy of the calculated slopes, and subsequently the identified force information, to be reduced. The calculated slope values and the corresponding identified force information are predicted to be accurate as long as the signal-to-noise ratio remains greater than about $100 : 1$. This limitation is addressed in the experimental verification by using accelerometers with sufficiently high sensitivity.

(iii) Impact Location

All of the calculated force information previously presented corresponds to impulsive loading near the center of the structure. In order to investigate the influence of the impact location on the accuracy of the calculated force information, the impact force is applied at a number of locations on the structure. The impact positions considered range from 1.43 ft (0.44 m) to 9.14 ft (2.79 m) from the end of the 18 ft (5.49 m) long structure. As a result of moving the impact location closer to the end of the structure, the reflections return to the impact location more quickly. The increase in error resulting from moving the impact location closer to the end of the structure is illustrated in Fig. 8.

The RMS error from the identified impulsive load and the average identified force values after the impact both increase as the impact position moves closer

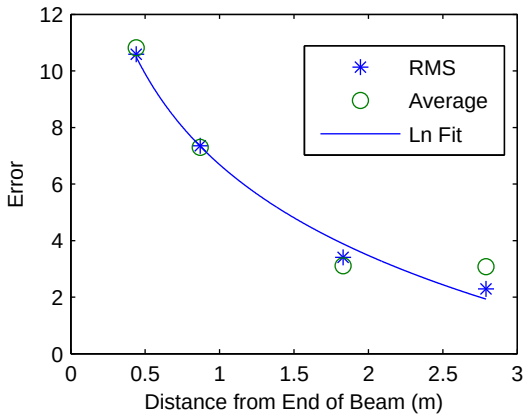

Figure 8: Force identification error with respect to the length of the structure. RMS error (*) during the impulsive load, average force (o) after the impulsive load, and a logarithmic curve (−) fit to the RMS error values are presented.

to the end of the structure. Because moving the impact location has the same effect as changing the length of the structure, i.e. reducing the length of time before the propagating wave returns to the impact location, the error values display the same logarithmic trend. In this case, the logarithmic curve fit to the RMS error values takes the form $Error = -4.636Ln\left(x_{impact}\right) + 6.6867$ with $R^2 = 0.9916$. When accounting for the fact that when the impact load is applied in the middle of the structure, the length over which the wave propagates before reflecting is half of the length of the structure, the data in Fig. 7 and Fig. 8 are very close to each other. While all of the conditions studied correspond to the same geometry and material properties, these factors influence the wave propagation speed and subsequently the length of time required for the propagating wave to be reflected and return to the impact location.

(iv) Impact Duration

Next, the influence of impact duration on the performance of the force identification method is studied. System responses are simulated for impulsive loads with half and twice the original duration. Changing the impact duration affects the response of the system in two significant ways. The first and most straightforward effect of changing the impact duration is that the amount of time between the end of the impulsive load and when the reflection returns the impact position is increased (reduced duration) or decreased (extended duration). The effect on the performance of the force identification method

will be similar to changing the distance between the impact position and the end of the structure. The second effect of changing the impact duration is that shorter/longer duration loads will contain a larger/smaller range of frequency content. Since the force identification method utilizes the SFEM, is it able to accommodate the higher frequency content and the change in the error results from the travel time of the propagating and then reflected wave. The two error measures for these conditions and the nominal case are presented in Fig. 9.

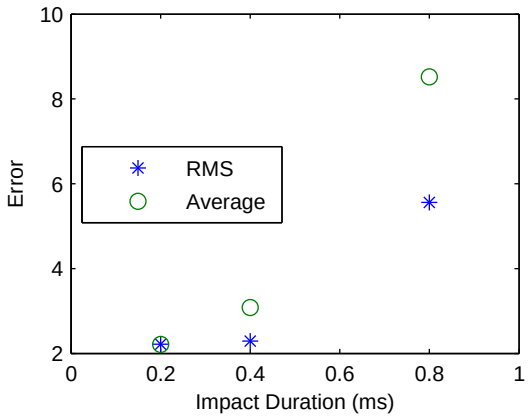

Figure 9: Force identification error with respect to the impulsive load duration. RMS error (*) during the impulsive load and average force (o) after the impulsive load are presented.

From the data presented in Fig. 9, it can be seen that for a shorter impact duration, the RMS error remains the same and the average force after the impact is slightly decreased. When the impact duration is increased to 0.8 ms, both error measures increase in value. The average force after the impact increases more the RMS error during the impact. However, these variations of the impact duration result in smaller increases in the error measures than the other parameters.

(v) Length of Response Data

The influence of the length of the response data on the accuracy of the reconstructed force is next studied. When less of the response data is available, the wave propagation data may not have fully decayed. This will require the application of more aggressive exponential windowing in order to reduce the response to zero by the end of the data set. When this is done, the influence of the exponential windowing on the data at the beginning of the data set which is used for the force identification process is more significantly affected.

This can increase the error in the identified force information. Properties such as damping and the boundary conditions of the structure can influence the length of time required for the propagating wave to decay and subsequently the length of the data set required to produce accurate results. In this study, these properties are kept constant and various lengths of response data are used to calculate the applied force. The error measures for the identified force information when using response data sets of lengths ranging from 5.12 s to down to 0.64 s are presented in Fig. 10.

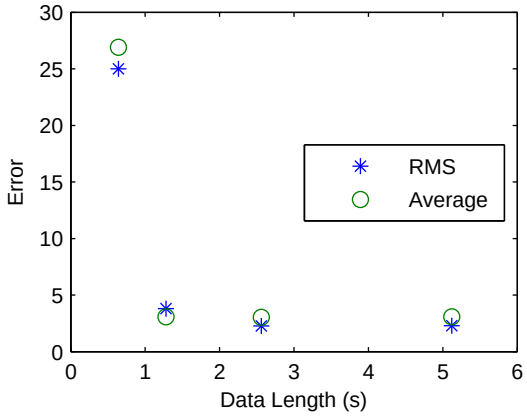

Figure 10: Force identification error with respect to the length of the response data. RMS error (*) during the impulsive load and average force (o) after the impulsive load are presented.

In this figure, it can be seen that above a threshold which lies between 0.64 s and 1.28 s, the error measures for the identified force information is close to the values for ideal conditions. However, after the length of the response data set is decreased to 0.64 s, both of the error measures increase by an order of magnitude. These results suggest that for a given set of conditions, a certain amount of time is required for the response of the structure to sufficiently decay in order for the force identification scheme to provide accurate results. Additionally, when the response data of length 0.64 s is used, the identified force information includes a consistent offset between the identified force values and the simulated force values, as shown in Fig. 11. Based upon the results of this numerical study, the presence of this characteristic in identified force information indicates that a longer amount of response data is required to improve the accuracy of the identified force.

Through this parametric study, the influence of (i) structure length, (ii)

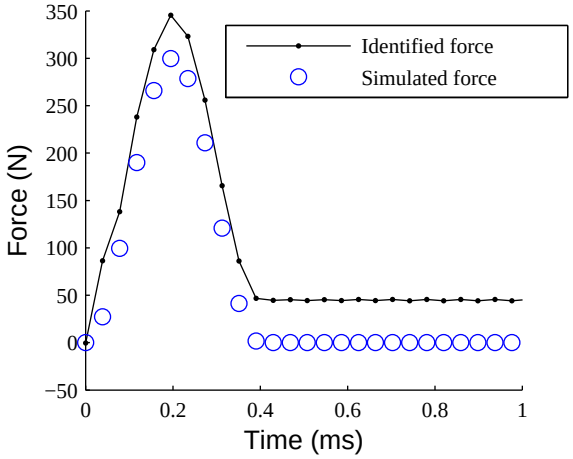

Figure 11: Identified (connected points) and simulated (circles) force information when only one quarter of the nominal length of the data set is used.

slope calculation, (iii) impact location, (iv) impact duration, and (v) length of response data on the performance of the force identification method was studied. The accuracy of the reconstructed impact force is qualitatively high comparing to previous works [26, 27, 29]. However, the variation in different case studies and measurement methods is a significant factor in the accuracy of the results. For instance, using calculated slope information in this work is a source of error specific to this work which can be enhanced by using gyro-sensors. Error in the identified force information was determined to increase for decreasing structure length, impacts applied closer to the end of the structure, longer impact durations, and when using response data with lengths below a system dependent threshold. The length of the response data was determined to have the potential to affect performance the most of the parameters studied. Changes to the structure length, impact location, and impact duration where determined to all have similar effects on the performance of the force identification method. When a signal-to-noise ratio of greater than 100 : 1 is maintained, the error introduced by the slope calculation is expected to be negligible.

3.4 Impact Location Identification

The force identification method reconstructs the impact force in terms of nodal forces. If the impact force is applied between the accelerometers, the distribu-

tion of the impact force is utilized to locate the impact location. A free-body diagram of the element with the applied impact force F and the nodal forces, F_1 and F_2, is shown in Fig. 12. By applying Newton's method, the summation of vertical forces and the summation of moments are calculated and presented in Eq. (38) and Eq. (39), respectively.

$$\sum F = F - F_1 - F_2 = m\ddot{V}_c, \tag{38}$$

$$\sum M_{cg} = \Delta M - F_1\frac{L}{2} + F_2\frac{L}{2} + F\left(\frac{L}{2} - x\right) = \frac{mL^2}{12}\ddot{\theta}_c. \tag{39}$$

where the mass of the element, displacement of the center of mass of the element, and the rotation of the element are represented by m, V_c, and θ_c, respectively. The impact force is applied at the distance x from the first node of the beam element of length L.

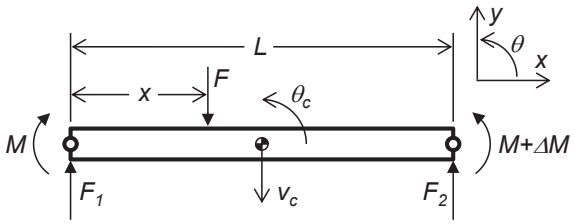

Figure 12: Free-body diagram of the beam element with the impact force F and the nodal forces, F_1 and F_2.

When the element is relatively short and the mass per length ρA of the beam is small, the mass of the element is relatively small and the inertial force can be considered negligible with respect to the applied force. For instance, the mass of a 3.43 in (8.71 cm) element of an Aluminum beam with a 1 in^2 (6.45 cm^2) cross section is 0.137 kg (weighing 1.34 N) which is quite small compared to the 300 N impact that is applied. By considering the mass of the element negligible, the equation for the summation of vertical forces is simplified to $F_1 + F_2 \approx F$.

When these assumptions are satisfied, the summation of the two nodal forces is equal to the applied impact force. As a result, it is possible to determine the impact force without knowledge of the exact location of the impact. This can significantly reduce the computational costs when compared to other approaches [27, 28, 29].

In order to calculate the impact location from the nodal forces, a straightforward nonlinear numerical solver is used. A flowchart illustrating the algo-

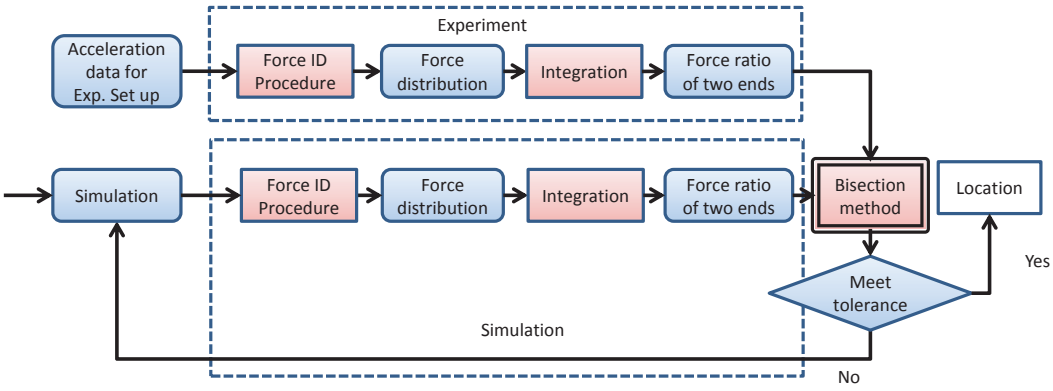

Figure 13: Flowchart of the location identification algorithm.

rithm used for location identification is presented in Fig. 13. The first step is to determine the distribution of the calculated impact force at the two ends of the element by using the experimental data collected from the accelerometers. The ratio of the impulses at the two neighboring accelerometers is used in this process. Then, simulations are performed with the beam model to produce response data for comparison. In order for this process to be effective, the model must accurately represent the structure. Known material properties and system geometry are used for the model and the damping parameter value is identified by comparing the simulated response of the model to the response of the experimental system. In the simulation portion of the process illustrated in Fig. 13, an extra node is added between the accelerometer positions for applying the impact force and predicting the response of the structure. However, only data from the nodes which correspond to the accelerometer locations are used in the location identification process. By using the ratio of the impulses for the experimental data and the simulation data, the location of the impact is calculated with the bisection method.

Although the relationship between the impulse ratio and the impact location is nonlinear, it is also a one-to-one relationship. This allows for the use of root-finding methods such as the bisection method. In order to start this process, two points are chosen close to the two nodes of the element on which the impact force was applied. The distance from the two starting points to the nodes is chosen to be 5% of the length of the element. This level of precision is selected as it corresponds to a practical limitation identified in the location identification procedure. The simulated impulse ratios for the two points are then compared to the impulse ratio for the experimental data. Based on the

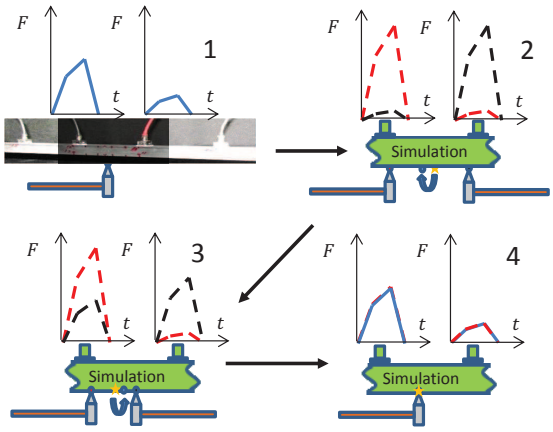

Figure 14: Implementation of the bisection method for the location identification process.

differences between these ratios, one of the initial points is discarded and a simulation is performed to obtain a simulated impulse ratio for a new point directly between the two initial points. The bisection method is continued in this way, as illustrated in Fig. 14, until the difference between the experimental impulse ratio and a simulated impulse ratio is less than the prescribed tolerance. The impact position used for the final simulated case provides the impact location for the experimental data.

The ratio of the identified impact forces at the two nodes adjacent to the impact location, calculated by using the simulation data, is shown in Fig. 15. These results are for a specific case and the details of this relationship are determined to be influenced by material properties, element length, and sampling frequency. In order to study the relationship between the impulse ratio and the location of the impact, the analytical model presented in Fig. 12 is revisited. By using the relationship between the impact force and nodal forces and similarly considering the rotational inertia to be negligible, Eq. (39) is simplified. If the deformation of the beam element is sufficiently small and the moment difference ΔM is considered negligible, an analytical formula for the impact force ratio is obtained. This formula, $F_1/F_2 = (x - L)/x$, provides the approximate ratio between the two nodal forces. The impact force ratio for these assumptions is plotted as a function of position in Fig. 15 along with impulse ratio data from numerical studies performed with the SFEM model of the beam structure. The analytical results qualitatively agree with the numerical results. The slight difference between the two is believed to result from

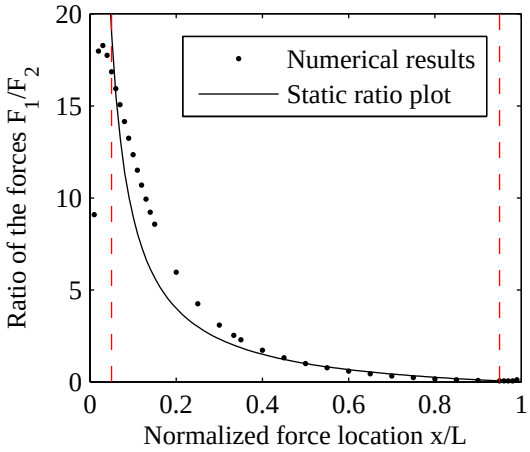

Figure 15: Impulse ratio as a function of impact location for the SFEM model ($\bullet$) and the analytical model ($-$). Red dashed lines indicate $\pm$ 5 % of location between nodes

neglecting the deformations of the beam element in the analytical model.

The impact force location identification process is applied to simulation results in order to study the method. Representative results are presented for a case where the impact force is applied between nodes 32 and 33 on the 18 ft (5.49 m) Aluminum beam at 20% of the element length ($0.2L$) from node 32. The force information calculated from the simulated response data is presented in Fig. 16. As anticipated, larger force values can be seen for the node closer to the impact location. By combining the force information, the identified impact force is calculated. These results, presented in Fig. 17, display strong agreement between the identified force and the simulated force without knowledge of the impact location. The RMS error for the impact and the average for the remainder of the 2 ms period shown in the figure are 2.98 N and 2.76 N, respectively. By analyzing the two calculated force curves presented in Fig. 16, an impulse ratio of 8.33 is calculated. The impact location is calculated to be at a distance of $0.19L$ from node 32. This corresponds to an error of 1% of the element length or 0.034 in (0.09 cm) on the 18 ft (5.49 m) beam structure.

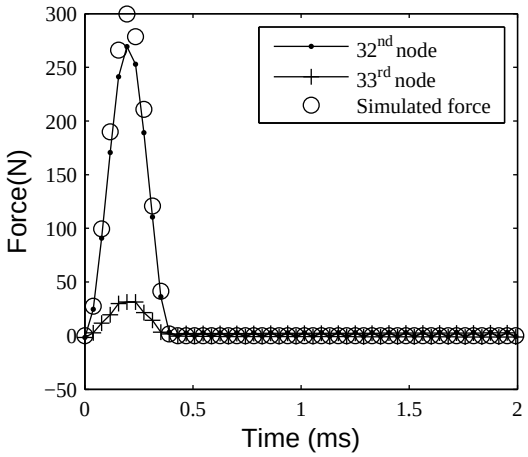

Figure 16: Force information calculated using simulation data. The force is applied at 20% of the element length from the 32^{nd} node.

4 Analysis & Discussion

In this section, AWT-FEM is used to numerically simulation nonlinear wave propagation in order to demonstrate the performance of the method. The performance of the force identification method is demonstrated by using experimentally collected data.

4.1 Modeling Nonlinear Wave Propagation

In the first subsection, simulations on a materially nonlinear rod are conducted by using AWT-FEM, AFT-FEM, and TFEM. The goal of this subsection is to demonstrate the advantages of AWT-FEM in fidelity and computational efficiency. Unlike beams or plates, which are strongly intrinsically dispersive, axial wave in a rod has an intact wave shape and it is easier to identify the existence of numerical errors. In the second subsection, simulations of a geometrically nonlinear beam by using AWT-FEM with physically realistic boundary conditions are conducted. The influence of the interaction with the boundaries on the response is analyzed. In the third subsection, simulations of a plate model with a weak geometric nonlinearity are presented to demonstrate the adaptability of the AWT-FEM for 2D models.

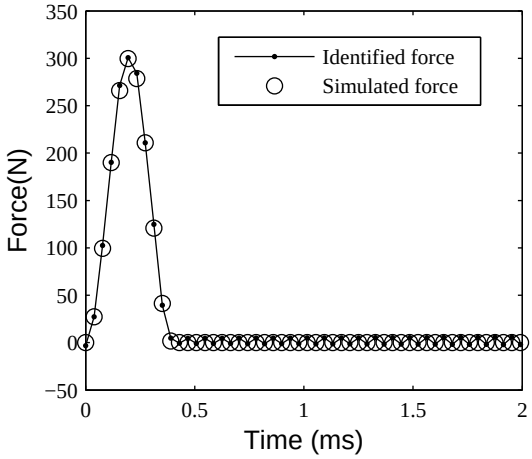

Figure 17: Summation of identified forces calculated using simulation data. The force is applied at 20% of the element length from the 32^{nd} node.

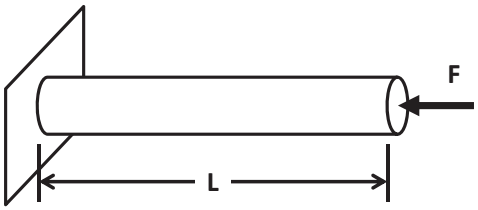

Figure 18: Diagram of a fixed-free rod.

4.1.1 Materially Nonlinear Rod

A diagram of a fixed-free rod subject to an axial impact load at one end is shown in Fig. 18. The parameters of the system are presented in Table. 2. The rod is modeled with a nonlinear constitutive relationship as defined in Eqn. (16) with a coefficient $\alpha = 20$.

Simulation results for the materially nonlinear rod model in Eqn. (17) with AWT-FEM, AFT-FEM, and TFEM are shown in Fig. 19. The Daubechies wavelet with an order of $N = 14$ is used for the spectrally-uncoupled wavelet transform and can yield sufficient smoothness in the responses. Fifty elements are used for the AWT-FEM and the AFT-FEM and 350 elements are used for the TFEM. For systems with physically realistic boundaries, additional damping combined with a longer time-window is required for the AFT-FEM

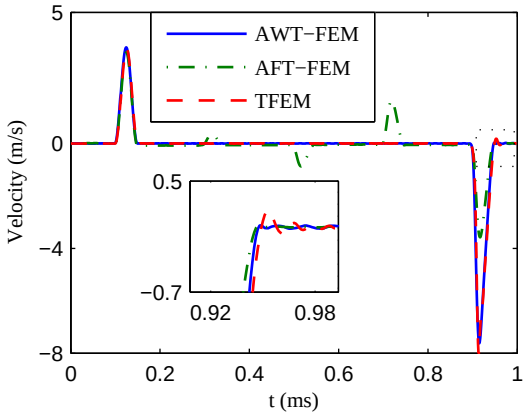

Figure 19: Velocity responses at the impacted position on the rod obtained by using AWT-FEM, AFT-FEM, and TFEM.

to avoid wrap-around errors. However, convergence issues can occur for the AFT-FEM iterative procedure with long time-window. In the simulation, the AFT-FEM is not able to produce a reliable physical response. In order to obtain a converged result for comparison with other methods, a large damping factor $\eta = 1 \times 10^4$ combined with the original time window is used.

An impulse in the velocity is created by the impact load at 0.1 ms. The wave is reflected by the fixed end and travels back to the impacted position at 0.9 ms. The wave shape in the reflected wave is shifted to the left-hand side. This distortion of wave shape caused by the nonlinearity is capture by all these three methods. Due to the additional damping, the amplitude response simulated by using AFT-FEM is severely reduced. Wrap-around errors also occurs in the time-history. These results demonstrate that the AFT-FEM cannot work for nonlinear structures without the use of non-reflecting boundaries. In order to leak the energy out of the system, either a long time window combined with artificial damping or a non-reflecting boundary at one end is needed. The high fidelity performance of the AFT-FEM is only possible with the help of these two mechanisms. In the comparison, a physical boundary is presented and the same time-window is adopted for all three numerical methods. The performance of AFT-FEM is greatly compromised. Due to the periodic nature of FFT, the traveling signal gets wrapped back into the reflected wave and results in periodic errors in the response. The TFEM can produce a response with adequate resolution at the expense of a refined meshing (350 elements). However, in the insert of Fig. 19, the reflected

Table 2: System parameters of rod.

Parameter	Value
Elastic modulus, E	70 GPa
Cross section, A	$\pi \times 25$ mm$\times$25 mm
Mass density, ρ	2800 kg/m^3
Rod length, L	2 m
Time window, T	1 ms
Impact duration, T_p	50 μs
Impact amplitude, T_a	100 kN
Sampling frequency, f	1000 kHz
Nonlinear coefficient, α	20

Table 3: Computation time.

AWT-FEM	AFT-FEM	TFEM
11.9 s	6.3 s	25.8 s

wave is affected by spurious oscillations late in the time series resulting from erroneously introduced numerical dispersion. For an impact load with shorter duration and higher frequency content, this error can be further magnified and completely distort the response [14]. On the contrary, the AWT-FEM only uses 50 elements to produce an intact wave response and capture the nonlinear distortion with high fidelity. The computation time for these three methods is listed in Table. 3. A Dell desktop with a Intel Core Quad CPU is used for all simulations. The parallel computing toolbox in $MATLAB$ is used to execute the calculation at different wavelet point in parallel. With the use of parallel computing, the AWT-FEM only uses 11.9 s with 50 elements to obtain an accurate response while the TFEM needs 25.8 s with 350 elements. The AFT-FEM cannot produce a correct response for these conditions. However, its fast computational performance indicates that if a fast numerical technique similar to FFT can be applied to modify the wavelet transform procedure, the computational performance of the AWT-FEM will be further improved.

A convergence study of the AWT-FEM and the TFEM is conducted. The same impact condition in Table. 2 is adopted. Simulations start with 1 elements and incrementally refine the mesh by adding 10 elements. The error is defined as the absolute value of the relative difference between the current simulation result of the velocity response V_{cur} and the reference in the previous state V_{pre} at the impacted position, as defined in Eqn. (40. The state

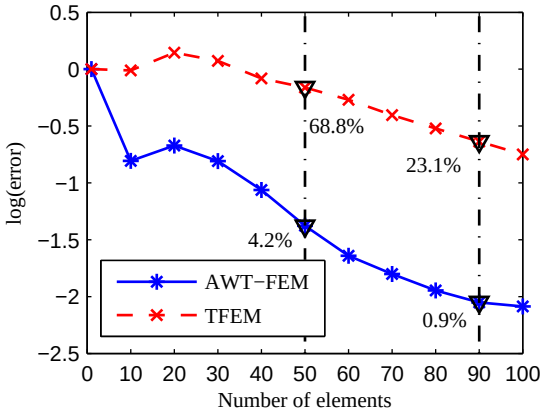

Figure 20: Comparison of convergence between the AWT-FEM and the nonlinear TFEM when the impact amplitude $T_a = 100$ kN and the nonlinear coefficient $\alpha = 20$.

being considered can be number of elements or order of Daubechies wavelet depending on the convergence study.)

$$Error = \frac{\sum_{i=1}^{n} \|V_{cur}(t_i) - V_{pre}(t_i)V\|}{\sum_{i=1}^{n} \|V_{cur}(t_i)V\|}. \tag{40}$$

As show in Fig. 20, the convergence performance of the AWT-FEM is significantly better than the TFEM. With 50 elements, the AWT-FEM has a 4.2% error level while the error of TFEM is 68.8%. By increasing the number of elements to 90, the AWT-FEM can reach a 0.9% error level while the TFEM still has an error of 23.1%.

A convergence study of the AWT-FEM with respect to the order of Daubechies wavelet is also conducted with the same error measure defined in Eqn. (40). As shown in Fig. 21, the order of Daubechies wavelet starts from 4 to 20 with an increment of 2. When the order is greater and equal to 8, the error level is below 1%.

4.2 Geometrically Nonlinear Beam

A diagram of a cantilevered beam with clamped-free boundaries is studied as shown in Fig. 22. A point impact load with amplitude 150 kN is applied at the

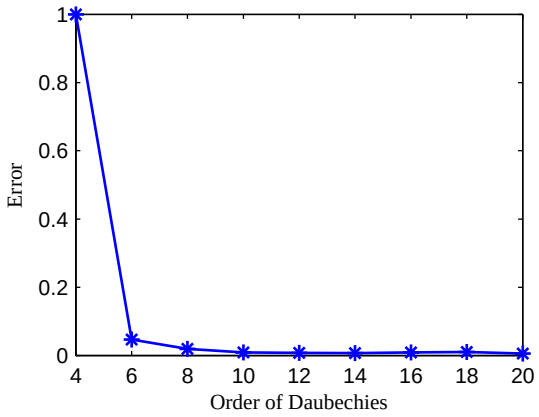

Figure 21: Convergence of the order of Daubechies wavelet.

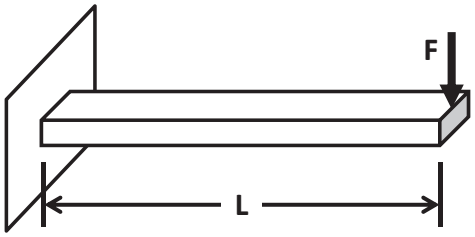

Figure 22: Diagram of a cantilevered beam.

free end. The parameters of the system are presented in Table 4. Simulations for a geometrically nonlinear beam model in Eqn. (21) and Eqn. (22) with the clamped-free boundaries is conducted by using AWT-FEM. A Daubechies wavelet with an order of $N = 14$ is used for the spectrally-uncoupled wavelet transform and can yield sufficient smoothness in the response. Fifty elements are used in the spectral element formulation to provide satisfactory accuracy and sufficient resolution.

A comparison of the velocity response at the impacted position obtained using the AWT-FEM and a nonlinear TFEM is shown in Fig. 23. The AWT-FEM uses 50 elements and the TFEM uses 100 elements. As reported in previous research, the geometric nonlinearities have limited influence on transverse wave propagation in beams in the intermediate strain regime [71, 72] compared to the nonlinear dispersion in the rod model. Since the beam is a strong intrinsically nonlinear system, the influence of the nonlinear dispersion introduced by

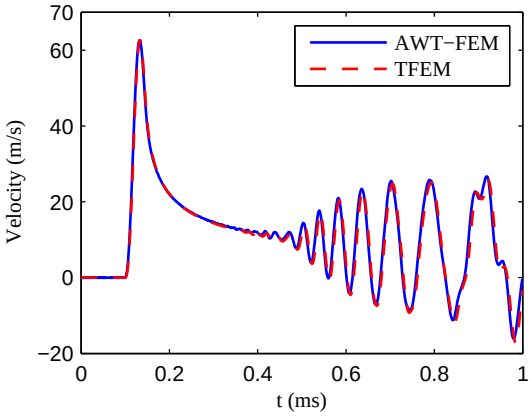

Figure 23: Velocity responses at the impacted position on the beam obtained by using AWT-FEM and TFEM.

geometric nonlinearity on the intrinsic dispersion relationship of the beam in the intermediate strain regime is negligible. The nonlinear responses obtained using two methods are close to each other. The difference in the later part of the response, where the reflected signal interacts with the forward traveling waves, may be attributed to the extra dispersion introduced by the TFEM.

A convergence study of the AWT-FEM and the TFEM for the beam model is conducted. The same impact condition in Table. 4 is adopted. Simulations start with 1 and 10 elements and incrementally refine the mesh by adding 10 elements. The error measure defined in Eqn. (40) is adopted here. The error level of the AWT-FEM is two orders of magnitude smaller than the TFEM. With 50 elements, the AWT-FEM has only 0.1% error while the TFEM has 3.8%. By increasing the number of elements to 90, the error of the AWT-FEM reduces to 0.04% while the TFEM is 0.2%.

A convergence study of the AWT-FEM with respect to the order of Daubechies wavelet is also conducted with the same error measure defined in Eqn. (40) for the beam model. As shown in Fig. 25, the order of Daubechies wavelet starts from 4 to 20 with an increment of 2. When the order is greater than and equal to 6, the error level is below 0.5%.

4.2.1 Geometrically Nonlinear Plate

A diagram of a cantilevered plate with clamped-free boundaries along the x dimension and free-free boundaries along the y dimension is shown in Fig. 26. A point impact load is applied at the middle point of edge BC (L_y). Other

Table 4: System parameters of a beam

Parameter	Value
Elastic modulus, E	70 GPa
Cross section, A	25 mm $\times$25 mm
Moment of inertia, I	3.26×10^{-8} m^4
Mass density, ρ	2800 kg/m^3
Beam length, L	1 m
Time window, T	1 ms
Impact duration, T_p	50 μs
Impact amplitude, T_a	100 kN
Sampling frequency, f	1000 kHz

Table 5: System parameters of a plate

Parameter	Value
Elastic modulus, E	70 GPa
Density, ρ	2800 kg/m^3
Length 1, L_x	1 m
Length 2, L_y	0.1 m
Thickness, h	25 mm
Poisson's ratio, ν	0.33
Time window, T	1 ms
Impact amplitude, F_m	100 kN
Impact duration, T_p	100 μs
Sampling frequency, f	500 kHz

general distributed load can also be chosen. The parameters of the system are presented in Table. 5. Along the y dimension, free-free boundaries have no constraints on the axial motion. Along the x dimension, the length is chosen to be $L_x = 1$ m, the same as was used for the beam model in previous subsection. The width is chosen to be $L_x = 0.1$ m to approximate a narrow 2D cantilever beam.

Simulations for a plate model with a weak geometric nonlinearity based on Eqn. (31) in the intermediate strain value regime is conducted by using AWT-FEM. A Daubechies wavelet with an order of $N = 22$ is used for the wavelet transform with respect to time. A Daubechies wavelet with an order of $N = 16$ with a sampling rate $\Delta y = 0.04$ m is used for the wavelet transform with respect to the spatial coordinate y. These wavelets are able to provide sufficient

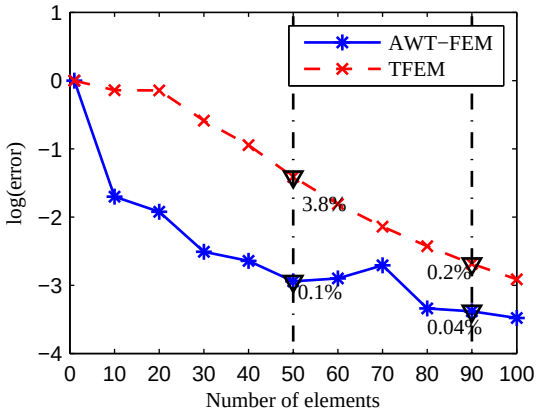

Figure 24: Comparison of convergence between the AWT-FEM and the nonlinear TFEM when the impact amplitude $T_a = 100$ kN

.

smoothness in the response. Twenty elements are used to approximate both the x dimension and the y dimension.

The comparison of the velocity responses at the impacted position obtained using the AWT-FEM, 1D TFEM, and 2D TFEM are shown in Fig. 27. The 1D TFEM with 100 elements is applied onto a 1D beam model with the same length as in the previous subsection. Since the width of the plate is narrow, the response of the AWT-FEM has a similar trend with the response of the 1D TFEM. There are three major differences between them. First, the width of the plate makes it stiffer than the corresponding 1D beam model, which results in a smaller amplitude of the response in the AWT-FEM. Second, the response in the AWT-FEM after the initial pulse includes small amplitude oscillations due to the interaction with reflected waves from both sides while the response in the 1D TFEM is smooth. Third, the later part of the responses in the two methods when the reflected waves travel back is different. This may be related to the effect of the sides of the plate and the influence of the different stiffnesses on the wave speed. A 2D TFEM with a 50×20 elements using ANSYS is also adopted here to produce the wave propagation process. As shown by the dashed-doted green line, the response is significantly different from the other two. For this problem with extreme impact loading, the 2D TFEM with a reasonable fine mesh using a sequential time integrator cannot produce a convergent result. It is also worth noting that by further increasing the impact load and leading the strain into a strong value regime, all three

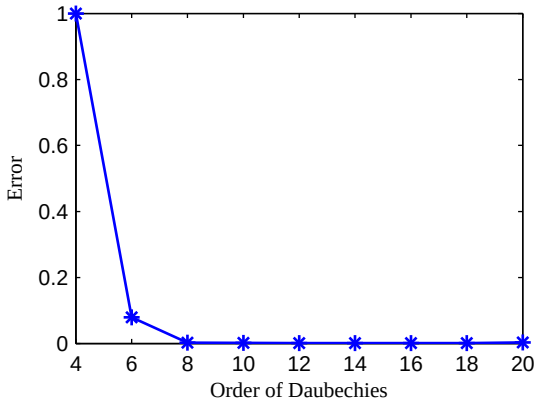

Figure 25: Convergence of the order of Daubechies wavelet.

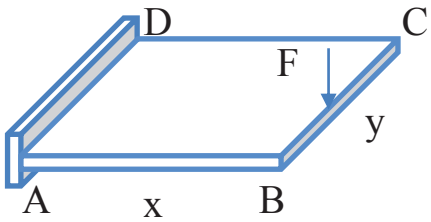

Figure 26: Diagram of a cantilevered plate.

methods will encounter convergence issue.

4.3 Force Identification

The performance of the force identification method is further studied with experimental response data in order to verify the performance observed by using simulated response data. The experimental setup is a 6 ft (1.83 m) long aluminum bar with a square cross-section and width of 1 in (25.4 mm), as shown in Fig. 28. It is shorter than the ideal beam structure defined in the numerical study in order to accommodate laboratory space limitations. The structure is instrumented with twenty-two PCB 356A22 accelerometers, with a frequency range of 0.5 to 4000 Hz, distributed evenly along its length. This number of accelerometers allows for good resolution in the slope information calculated from the acceleration data. These are triaxial accelerometers (axial, transverse and lateral directions), but only transverse response data is used.

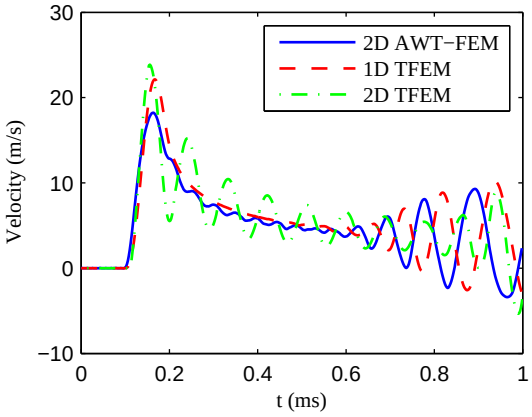

Figure 27: Velocity responses at the impacted position on the beam obtained using AWT-FEM, 1D TFEM, and 2D TFEM.

The acceleration data is collected with a sampling frequency of 102.4 kHz in order to capture the response with good temporal resolution. The data is down-sampled by a factor of four in order to accommodate memory limitations when applying the force identification procedure. The structure is suspended from bungee cords in order to approximate free-free boundary conditions. A PCB 086D05 modal impact hammer is used to apply impulsive loads in the vertical direction. The applied force is measured by the force transducer in the impact hammer for comparison with the identified force information. For transducer signal conditioning and A/D signal conversion, a LMS SCADAS III acquisition system is used. The measured data is recorded by using LMS Test.Lab Software, Ver. 11A. The acceleration data sets are chosen from the accelerometers in the vicinity of the impact location. The acceleration data contains the response signal of the structure due to the impact and also the reflections due to the boundaries of the structure. The acceleration data is dispersive due to the dispersive nature of the structure.

The impact force identification method is applied to experimental response data collected for conditions when the impact location is collocated with an accelerometer and when the impact is applied between accelerometers. Representative results for these conditions are presented and discussed below.

As it was shown in the parametric study, the calculated impact force is more precise at cases where the impact occurs close to the middle of the structure. The first data set presented corresponds to an impact force being applied to the experimental system at the location of accelerometer number 11

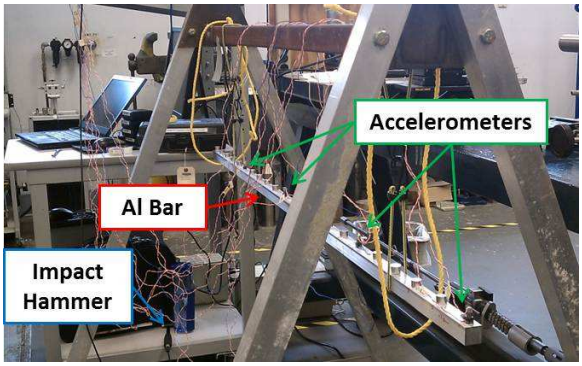

Figure 28: Photograph of the experimental setup.

near the middle of the structure. The force information obtained by applying the force identification method is presented in Fig. 29. Since the impact force was applied at the location of the accelerometer, the location of the impact is easily identified as the position of accelerometer 11. The identified force information agrees well with the measured force, successfully capturing the qualitative characteristics of the impulsive load. However, some discrepancies are observed. This error is believed to be introduced as a result of errors in the slope calculation due to signal noise and also due to the low frequency stop-band of the accelerometers which are used to perform modal analysis. The RMS error for this case is 34.60 N and an average value of 10.45 N exists during the remainder of the 1 ms time window presented in Fig. 29. In comparison with the ideal conditions, the length of the beam is shorter and noise is present in the acceleration data. While each of these differences contributes to the reduced accuracy of the calculated force information, the RMS error for the impulsive load is only 12% of the maximum force value.

The next two data sets presented were collected when the impact force was applied between accelerometers. These data sets are used in order to test the force identification as well as the location identification methods. The impact force identification method is applied to calculate the forces applied to the structure and the location identification method is used to determine where the impact force was applied. The first of these two data sets correspond to conditions where the impact force is applied at the center between accelerometers 11 and 12. The impact force information obtained from the force identification method is presented in Fig. 30. The detected force values at nodes 11 and 12 exhibit similar properties since the impact was applied at equal distances from the two accelerometers. However, after the impulsive

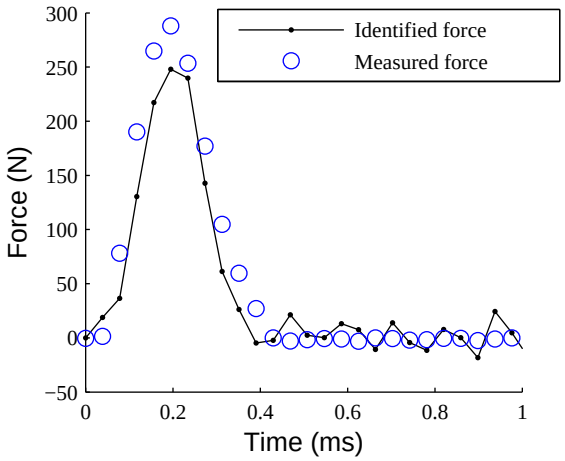

Figure 29: Force information calculated from the experimental data, force applied at node 11.

load, the identified force values increase or decrease linearly with time.

The summation of the identified forces at the accelerometers on either side of the impact location provides the identified force. The identified force information (Δ) agrees well with the measured force information (o) during the impact. After the impact, the calculated force exhibits a persistent offset from the measured force values. The RMS error for the summation of the two calculated forces is 39.20 N during the impact and averages 53.21 N during the remainder of the 1 ms. Based on the parametric study, the force offset after the impact is believed to be due to the short length of the acceleration data set. Access to a longer set of the response data is expected to yield more accurate results. The bungee cords supporting the experimental system also apply a small but constant force to the structure which is not addressed in the model and may influence the results. By using the impulse ratio calculated for the force values at accelerometers 11 and 12, the impact location is calculated to be at a distance of $0.52L$ from accelerometer 11. This corresponds to a deviation of only 2% of the distance between the accelerometers which is less than 2 mm.

The final data set correspond to conditions where the impact force is applied at a distance of $0.40L$ from accelerometer 11. The impact force information obtained from the force identification method is presented in Fig. 31. As the numerical study predicted, the calculated force values for the accelerometer nearest to the impact location are larger than the values for the other

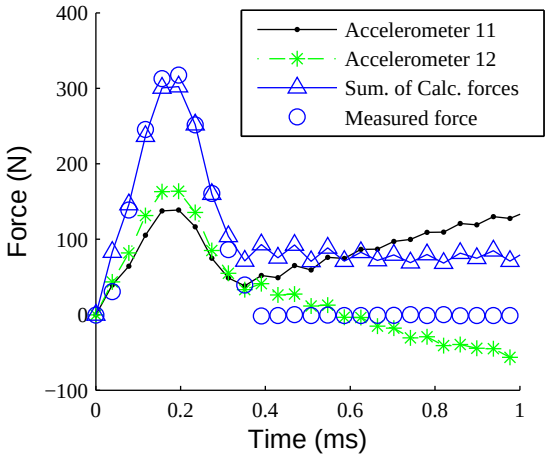

Figure 30: Force information calculated using experimental data for the force applied at 50% of the distance between the accelerometers from accelerometer 11.

location. Again, the calculated force values at the positions of the two accelerometers gradually increase or decrease after the impact. The identified force information is obtained from the summation of the calculated forces and it agrees well with the measured force during the impact. The RMS error is 35.61 N during the impact and averages 83.78 N during the remainder of the 1 ms presented in Fig. 31. The impact force is identified to be at a distance of $0.37L$ from accelerometer 11. This corresponds to a deviation of only 3% of the distance between the accelerometers which is less than 3 mm from the actual location of the applied impact force. Considering the fact that the impact was manually applied and the hammer tip is 6 mm wide, the errors in the results of the location identification method are acceptable.

The experimental verification illustrates a good agreement between the experiment and the simulation predictions. However, the force identification method of the experimental setup might experience errors due to the discrepancies in the material properties, loading conditions, mass of accelerometers and other different unknown factors. These errors can be reduced by conducting different tests in order to calibrate the method.

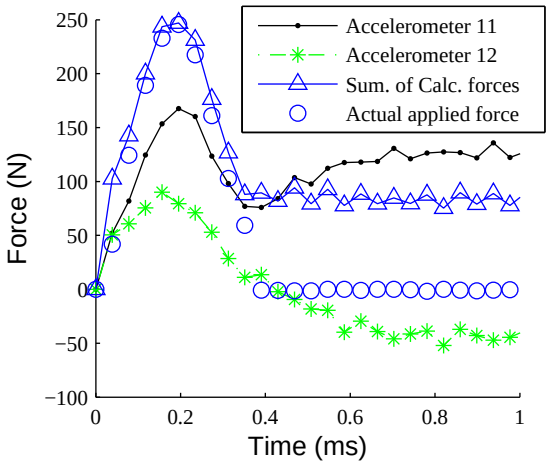

Figure 31: Force information calculated using experimental data for the force applied at 40% of the distance between the accelerometers from accelerometer 11.

5 Closure

In this work, numerical simulation and force identification & localization methods were developed to facilitate the high-fidelity study of nonlinear wave propagation caused by extreme impact loading conditions. By using a wavelet-based spectral finite element method and an alternating wavelet-time framework, the linear method was adapted for nonlinear systems. The alternating wavelet-time finite element method (AWT-FEM) is demonstrated to provide high-fidelity results, be compatible with parallel computing, and provide a means to study general nonlinear behavior in a range of simple structures. The direct iteration algorithm adopted in this study limits the convergence performance of the AWT-FEM. For 1D beam and 2D plate with geometric nonlinearity, the AWT-FEM is able to obtain a converged response within an intermediate strain value regime (10^{-6} to 10^{-3}) where the influence of the geometric nonlinearity is limited. In order to address this issue, a modified Newton-Raphson iterative method was subsequently developed to replace the direct iteration algorithm in order to improve the convergence performance of the AWT-FEM and facilitate its application for large deformation problems.

An impact force identification method using the spectral finite element method was also presented and demonstrated with a beam structure. With this method, the impact force can be determined without precise information about the location of the impact on the structure. The procedure was demonstrated

with simulated response data for propagating mechanical waves and validated by using experimental data. In simulations, excellent agreement was observed for nominal conditions. Sources of error in the identified force information were investigated through a parametric study. The most influential parameter in the force calculation procedure is the length of the response data set. Reduced performance was identified when decreasing the structure length, moving the impact location toward the end of the structure, and increasing the impact duration. Also, the trends associated with varying the structure length, impact position, and impact duration were studied. The force identification method was also applied to experimental data and was able to successfully identify the characteristics of the impact and provide identified impact force information with relatively low error. In conjunction with the force identification method, a new technique for accurately determining the location of the impact was proposed. When applied to experimental data, the impact locations were identified within 5% of the distance between the accelerometers from the actual location, which corresponds to an error of less than 0.17 in (0.4 cm) on a 6 ft (1.83 m) structure.

The AWT-FEM is promising tool with great potential for studying a wide range of nonlinear wave propagation in various structural components. While the numerical studies conducted in this work provided great insight into the performance of the new numerical simulation technique, future studies will incorporate significant experimental verification in order to further study and refine the tool. Future work on the new methods for force identification and localization will explore the offset in the calculate force information which follows the impulsive load. Further refinements to the force identification methods will also include incorporating more advanced sensor technology, such as gyroscopic sensors to directly measure rotational response information. While these force identification methods have been demonstrated for beam structures, its application to structures such as rods, plates, and more complicated structures such as shells, trusses and arches will also be explored.

Acknowledgments

The PI gratefully acknowledges the support received through AFOSR Grant No. FA9550-11-1-0108 under the direction of program manager Dr. David Stargel.

References

[1] P. Taylor and C. Ford. Simulation of blast-induced early-time intracranial wave physics leading to traumatic brain injury. *Journal of Biomechanical Engineering*, 131(6):61007–61018, 2009.

[2] M. Meo and G. Zumpano. Nonlinear elastic wave spectroscopy identification of impact damage on a sandwich plate. *Composite structures*, 71(3-4):469–474, 2005.

[3] Paul A Johnson and Xiaoping Jia. Nonlinear dynamics, granular media and dynamic earthquake triggering. *Nature*, 437(7060):871–874, 2005.

[4] YA Khulief and H Al-Naser. Finite element dynamic analysis of drillstrings. *Finite elements in analysis and design*, 41(13):1270–1288, 2005.

[5] José M Carcione, Flavio Poletto, and Giorgia Pinna. Simulation of flexural waves in drill pipes including the effects of the gravitational field: Flexural waves and effects of gravity. *Wave Motion*, 50(2):310–325, 2012.

[6] Gabriel Piras, WL Cleghorn, and JK Mills. Dynamic finite-element analysis of a planar high-speed, high-precision parallel manipulator with flexible links. *Mechanism and Machine Theory*, 40(7):849–862, 2005.

[7] J. Doyle. *Wave Propagation in Structures*. Springer, Berlin, Germany, 1997.

[8] A. Nayfeh and D. Mook. *Nonlinear oscillations*. John Wiley, New York, USA, 1995.

[9] J. Reddy. *An introduction to nonlinear finite element analysis*. Oxford University Press, Oxford, UK, 2004.

[10] S. Ham and K. Bathe. A finite element method enriched for wave propagation problems. *Computers and structures*, 94-95:1–12, 2012.

[11] J. Doyle. A spectrally formulated finite element for longitudinal wave propagation. *International Journal of Analytical and Experimental Modal Analysis*, 3:1–5, 1988.

[12] Mira Mitra and S Gopalakrishnan. Spectrally formulated wavelet finite element for wave propagation and impact force identification in connected 1-d waveguides. *International journal of solids and structures*, 42(16):4695–4721, 2005.

[13] Thomas JR Hughes and Gregory M Hulbert. Space-time finite element methods for elastodynamics: formulations and error estimates. *Computer methods in applied mechanics and engineering*, 66(3):339–363, 1988.

[14] A. Idesman. A new high-order accurate continuous galerkin method for linear elastodynamics problems. *Computational Mechanics*, 40(2):261–279, 2007.

[15] P. Kudela, M. Krawczuk, and W. Ostachowicz. Wave propagation modelling in 1d structures using spectral finite elements. *Journal of Sound and Vibration*, 300(1):88–100, 2007.

[16] Anthony T Patera. A spectral element method for fluid dynamics: laminar flow in a channel expansion. *Journal of Computational Physics*, 54(3):468–488, 1984.

[17] A. Ramabathiran and S. Gopalakrishnan. Time and frequency domain finite element models for axial wave analysis in hyperelastic rods. *Mechanics of advanced materials and structures*, 19(1-3):79–99, 2012.

[18] Srinivasan Gopalakrishnan, Abir Chakraborty, and D Roy Mahapatra. *Spectral Finite Element Method: Wave Propagation, Diagnostics and Control in Anisotropic and Inhomogenous Structures*. Springer, London, UK, 2008.

[19] Usik Lee. *Spectral element method in structural dynamics*. Wiley, Chichester, UK, 2009.

[20] John R Williams and Kevin Amaratunga. A discrete wavelet transform without edge effects using wavelet extrapolation. *Journal of Fourier Analysis and Applications*, 3(4):435–449, 1997.

[21] S Gopalakrishnan and Mira Mitra. *Wavelet methods for dynamical problems: With application to metallic, composite, and nano-composite structures*. CRC Press, New York, USA, 2010.

[22] L Pahlavan, C Kassapoglou, ASJ Suiker, and Z Gürdal. A 2d wavelet-based spectral finite element method for elastic wave propagation. *Philosophical Magazine*, 92(28-30):3699–3722, 2012.

[23] Lotfollah Pahlavan, Christos Kassapoglou, and Zafer Gürdal. Spectral formulation of finite element methods using daubechies compactly-supported wavelets for elastic wave propagation simulation. *Wave Motion*, 50(3):558–578, 2012.

[24] T. Cameron and J. Griffin. An alternating frequency/time domain method for calculating the steady-state response of nonlinear dynamic systems. *Journal of applied mechanics*, 56(1):149–154, 1989.

[25] U. Lee and I. Jang. Nonlinear spectral element model for the blood flow in human arteries. In *Proceedings of the 2011 International Symposium of Computational Models for Life Sciences*, pages 136–145. Toyama City, Japan, 2011.

[26] J F Doyle. An experimental method for determining the dynamic contact law. *Experimental Mechanics*, 24(1):10–16, 1984.

[27] D E Adams, B Zwink, and N C Yoder. Impact loading and damage identification using minimal dynamic sensing strategies. *SAMPE, Long Beach, CA*, 2008.

[28] N Hu and H Fukunaga. A new approach for health monitoring of composite structures through identification of impact force. *Journal of Advanced Science*, 17(1-2):82–89, 2005.

[29] G Yan and L Zhou. Impact load identification of composite structure using genetic algorithms. *Journal of Sound and Vibration*, 319(3-5):869–884, 2009.

[30] P E Hollandsworth and H R Busby. Impact force identification using the general inverse technique. *International Journal of Impact Engineering*, 8(4):315–322, 1989.

[31] V I Bateman, T G Carne, D L Gregory, S W Attaway, and H R Yoshimura. Force reconstruction for impact tests. *Journal of Vibration and Acoustics*, 113(2):192–201, 1991.

[32] J F Doyle. Further developments in determining the dynamic contact law. *Experimental Mechanics*, 24(4):265–270, 1984.

[33] C Chang and C T Sun. Determining transverse impact force on a composite laminate by signal deconvolution. *Experimental Mechanics*, 29(4):414–419, 1989.

[34] V Calhoun, X Golay, and G Pearlson. Improved fMRI slice timing correction: interpolation errors and wrap around effects. In *Proceedings, ISMRM, 9th Annual Meeting, Denver*, page 810, 2000.

[35] S Liu, Q Wang, and G Liu. A versatile method of discrete convolution and FFT (DC-FFT) for contact analyses. *Wear*, 243(1):101–111, 2000.

[36] Y Keller, A Averbuch, and M Israeli. Pseudopolar-based estimation of large translations, rotations, and scalings in images. *Image Processing, IEEE Transactions on*, 14(1):12–22, 2005.

[37] J F Doyle. An experimental method for determining the location and time of initiation of an unknown dispersing pulse. *Experimental Mechanics*, 27(3):229–233, 1987.

[38] C Chen and F G Yuan. Impact source identification in finite isotropic plates using a time-reversal method: theoretical study. *Smart Materials and Structures*, 19(10):105028, 2010.

[39] E Wu, J C Yeh, and C S Yen. Impact on composite laminated plates: an inverse method. *International Journal of Impact Engineering*, 15(4):417–433, 1994.

[40] L Gaul and S Hurlebaus. Identification of the impact location on a plate using wavelets. *Mechanical Systems and Signal Processing*, 12(6):783–795, 1998.

[41] T Kundu, S Das, S A Martin, and K V Jata. Locating point of impact in anisotropic fiber reinforced composite plates. *Ultrasonics*, 48(3):193–201, 2008.

[42] J H Park and Y H Kim. Impact source localization on an elastic plate in a noisy environment. *Measurement Science and Technology*, 17(10):2757, 2006.

[43] M Meo, G Zumpano, M Piggott, and G Marengo. Impact identification on a sandwich plate from wave propagation responses. *Composite Structures*, 71(3):302–306, 2005.

[44] D Liang, S-F Yuan, and M-L Liu. Distributed coordination algorithm for impact location of preciseness and real-time on composite structures. *Measurement*, 46(1):527–536, 2013.

[45] R Seydel and F K Chang. Impact identification of stiffened composite panels: I. system development. *Smart Materials and Structures*, 10(2):354, 2001.

[46] N Hu, H Fukunaga, S Matsumoto, B Yan, and X H Peng. An efficient approach for identifying impact force using embedded piezoelectric sensors. *International Journal of Impact Engineering*, 34(7):1258–1271, 2007.

[47] J Park, S Ha, and F K Chang. Monitoring impact events using a system-identification method. *AIAA journal*, 47(9):2011–2021, 2009.

[48] Z Boukria, P Perrotin, and A Bennani. Experimental impact force location and identification using inverse problems: application for a circular plate. *International Journal of Mechanics*, 5(1):48–55, 2011.

[49] K Shin, H Yang, S-K Lee, and Y-S Lee. Group delay based location template matching method for the identification of the impact location on a plate. *Journal of Sound and Vibration*, 332(8):2111–2117, 2013.

[50] P Ghaderi, A J Dick, J R Foley, and G Falbo. High fidelity force location identification in beam structures. In *83rd Shock and Vibration Symposium*, New Orleans, Louisiana, USA, November 4-8 2012.

[51] Y Liu, P Ghaderi, and A J Dick. A semi-analytical nonlinear spectral finite element method for one-dimensional waveguides. In *ASME International Mechanical Engineering Congress and Exposition (IMECE)*, 2012.

[52] P Ghaderi, A J Dick, J R Foley, and G Falbo. *Topics in Nonlinear Dynamics, Volume 3*, chapter Spectral Domain Force Identification of Impulsive Loading in Beam Structures, pages 157–165. Springer, 2012.

[53] Y Liu and A J Dick. Numerical simulation of lateral impact wave propagation in drill-strings. In *2013 CAPA Petroleum and Petrochemical Technical Symposium*, Houston, Texas, USA, October 25 2013.

[54] Y Liu and A J Dick. Nonlinear analysis of transient wave propagation in beam structures using aft-fem. In *ASME International Mechanical Engineering Congress & Exposition (IMECE)*, San Diego, California, USA, November 15-21 2013.

[55] P Ghaderi, S Rich, and A J Dick. Spectral domain based impact force identification for rod structures. In *ASME International Mechanical Engineering Congress & Exposition (IMECE)*, San Diego, California, USA, November 15-21 2013.

[56] Y Liu and A J Dick. Numerical analysis of lateral wave propagation in drill-string for stability monitoring. In *ASME International Mechanical Engineering Congress & Exposition*, Montreal, Quebec, Canad, November 14-20 2014.

[57] Y Liu and A J Dick. *Topics in Modal Analysis II, Volume 8*, chapter On the Role of Boundary Conditions in the Nonlinear Dynamic Response of Simple Structures, pages 135–143. Springer, 2014.

[58] Y Liu, A J Dick, J Dodson, and J Foley. *Topics in Modal Analysis II, Volume 8*, chapter Nonlinear High Fidelity Modeling of Impact Load Responses in a Rod, pages 129–134. Springer, 2014.

[59] Y Liu and A J Dick. 'wave propagation in a materially nonlinear rod: Numerical and experimental investigations. In *IMAC XXXIII A Conference and Exposition on Structural Dynamics*, Orlando, Florida, USA, February 2-5 2015.

[60] Y Liu, Y Ji, and A J Dick. Numerical investigation of lateral and axial wave propagations in drill-string for stability monitoring. *Journal of Vibration and Acoustics*, 2015. DOI: 10.1115/1.4029992.

[61] Y Liu and A J Dick. High fidelity analysis of transient wave propagation in nonlinear one-dimensional waveguides. *Journal of Computational and Nonlinear Dynamics*, 2015. DOI: 10.1115/1.4028015.

[62] Y Liu and A J Dick. Alternating frequency-time finite element method: High-fidelity modeling of nonlinear wave propagation in one-dimensional waveguides. *Journal of Computational and Nonlinear Dynamics*, in review.

[63] P Ghaderi, A J Dick, J R Foley, and G Falbo. Practical high-fidelity frequency-domain force and location identification. *Computers and Structures*, in review.

[64] Y Liu and A J Dick. Alternating wavelet-time finite element method: Modeling and analysis of nonlinear wave propagation in one- and two-dimensional waveguides. *Journal of Sound and Vibration*, in review.

[65] Y Liu and A J Dick. Nonlinear wave propagation in one-dimensional structures: Analysis and force identification. *Journal of Computational and Nonlinear Dynamics*, in review.

[66] Gregory Beylkin. On the representation of operators in bases of compactly supported wavelets. *SIAM Journal on Numerical Analysis*, 29(6):1716–1740, 1992.

[67] J. Li and Y. Zhang. Exact travelling wave solutions in a nonlinear elastic rod equation. *Applied Mathematics and Computation*, 202(2):504–510, 2008.

[68] T von Kármán. Fesigkeitsprobleme in maschinenbau. *Encycl de Math Wiss*, 4:348–351, 1910.

[69] W Fladung and R Rost. Application and correction of the exponential window for frequency response functions. *Mechanical Systems and Signal Processing*, 11(1):23–36, 1997.

[70] J F Doyle. *Wave Propagation in Structures: Spectral Analysis Using Fast Discrete Fourier Transforms*. Springer, New York, NY, 1997.

[71] Mohammad H Abedinnasab and Mahmoud I Hussein. Wave dispersion under finite deformation. *Wave Motion*, 50(3):374–388, 2013.

[72] Heming Xu, Steven M Day, and Jean-Bernard H Minster. Hysteresis and two-dimensional nonlinear wave propagation in berea sandstone. *Journal of Geophysical Research: Solid Earth (1978–2012)*, 105(B3):6163–6175, 2000.

1.

1. Report Type

Final Report

Primary Contact E-mail

Contact email if there is a problem with the report.

andrew.j.dick@rice.edu

Primary Contact Phone Number

Contact phone number if there is a problem with the report

713-348-5259

Organization / Institution name

Rice University

Grant/Contract Title

The full title of the funded effort.

Modeling and Analysis Tools for Linear and Nonlinear Mechanical Systems Subjected to Extreme Impulsive Loading

Grant/Contract Number

AFOSR assigned control number. It must begin with "FA9550" or "F49620" or "FA2386".

FA9550-11-1-0108

Principal Investigator Name

The full name of the principal investigator on the grant or contract.

Andrew Dick

Program Manager

The AFOSR Program Manager currently assigned to the award

David Stargel

Reporting Period Start Date

07/01/2011

Reporting Period End Date

06/30/2014

Abstract

The extreme impact loading (high amplitude and short durations) can result in wave propagation with significant nonlinear characteristics. The focus of this work was the development of high fidelity modeling and analysis methods for studying this nonlinear behavior. The Alternating Frequency-Time Finite Element Method was developed from the spectral finite element method (SFEM) in order to expand its high fidelity performance to study nonlinear wave propagation. Later efforts produced the Alternating Wavelet-Time Finite Element Method by using a wavelet basis. A practical force identification scheme was also developed by using SFEM to determine both temporal and spatial information about an impact load by using only a small number of sensors. The force identification scheme was also developed by using SFEM to determine both temporal and spatial information about an impact load by using only a small number of sensors. These numerical simulation techniques and force identification methods provide the means to gain new insight into the effects of extreme impact loading on structures. This improved understanding can be used to design new structures and to better understand how they

will perform under severe conditions.

Distribution Statement

This is block 12 on the SF298 form.

Distribution A - Approved for Public Release

Explanation for Distribution Statement

If this is not approved for public release, please provide a short explanation. E.g., contains proprietary information.

SF298 Form

Please attach your SF298 form. A blank SF298 can be found here. Please do not password protect or secure the PDF The maximum file size for an SF298 is 50MB.

AFD-070820-035.pdf

Upload the Report Document. File must be a PDF. Please do not password protect or secure the PDF . The maximum file size for the Report Document is 50MB.

Final_Report_FA9550-11-1-0108.pdf

Upload a Report Document, if any. The maximum file size for the Report Document is 50MB.

Archival Publications (published) during reporting period:

[1] P Ghaderi, A J Dick, J R Foley, and G Falbo. High fidelity force location identification in beam structures. In 83rd Shock and Vibration Symposium, New Orleans, Louisiana, USA, November 4-8 2012.

[2] Y Liu, P Ghaderi, and A J Dick. A semi-analytical nonlinear spectral finite element method for one-dimensional waveguides. In ASME International Mechanical Engineering Congress and Exposition (IMECE), 2012.

[3] P Ghaderi, A J Dick, J R Foley, and G Falbo. Topics in Nonlinear Dynamics, Volume 3, chapter Spectral Domain Force Identification of Impulsive Loading in Beam Structures, pages 157–165. Springer, 2012.

[4] Y Liu and A J Dick. Numerical simulation of lateral impact wave propagation in drill-strings. In 2013 CAPA Petroleum and Petrochemical Technical Symposium, Houston, Texas, USA, October 25 2013.

[5] Y Liu and A J Dick. Nonlinear analysis of transient wave propagation in beam structures using aft-fem. In ASME International Mechanical Engineering Congress & Exposition (IMECE), San Diego, California, USA, November 15-21 2013.

[6] P Ghaderi, S Rich, and A J Dick. Spectral domain based impact force identification for rod structures. In ASME International Mechanical Engineering Congress & Exposition (IMECE), San Diego, California, USA, November 15-21 2013.

[7] Y Liu and A J Dick. Numerical analysis of lateral wave propagation in drillstring for stability monitoring. In ASME International Mechanical Engineering Congress & Exposition, Montreal, Quebec, Canad, November 14-20 2014.

[8] Y Liu and A J Dick. Topics in Modal Analysis II, Volume 8, chapter On the Role of Boundary Conditions in the Nonlinear Dynamic Response of Simple Structures, pages 135–143. Springer, 2014.

[9] Y Liu, A J Dick, J Dodson, and J Foley. Topics in Modal Analysis II, Volume 8, chapter Nonlinear High Fidelity Modeling of Impact Load Responses in a Rod, pages 129–134. Springer, 2014.

[10] Y Liu and A J Dick. ‘wave propagation in a materially nonlinear rod: Numerical and experimental investigations. In IMAC XXXIII A Conference and Exposition on Structural Dynamics, Orlando, Florida, USA, February 2-5 2015.

[11] Y Liu, Y Ji, and A J Dick. Numerical investigation of lateral and axial wave propagations in drill-string for stability monitoring. Journal of Vibration and Acoustics, 2015. DOI: 10.1115/1.4029992.

[12] Y Liu and A J Dick. High fidelity analysis of transient wave propagation in nonlinear

one-dimensional waveguides. Journal of Computational and Nonlinear Dynamics, 2015. DOI: 10.1115/1.4028015.

Changes in research objectives (if any):

Change in AFOSR Program Manager, if any:

Extensions granted or milestones slipped, if any:

AFOSR LRIR Number

LRIR Title

Reporting Period

Laboratory Task Manager

Program Officer

Research Objectives

Technical Summary

Funding Summary by Cost Category (by FY, $K)

	Starting FY	FY+1	FY+2
Salary			
Equipment/Facilities			
Supplies			
Total			

Report Document

Report Document - Text Analysis

Report Document - Text Analysis

Appendix Documents

2. Thank You

E-mail user

Mar 16, 2015 13:57:14 Success: Email Sent to: andrew.j.dick@rice.edu